

# Using radiant intensity to characterize the anisotropy of satellite-derived city light at night



Xi Li <sup>a,\*</sup>, Xiaoyu Shang <sup>a</sup>, Qingling Zhang <sup>b</sup>, Deren Li <sup>a</sup>, Fengrui Chen <sup>c</sup>, Minghui Jia <sup>a</sup>, Yan Wang <sup>a</sup>

<sup>a</sup> State Key Laboratory of Information Engineering in Surveying, Mapping and Remote Sensing, Wuhan University, Wuhan, China

<sup>b</sup> School of Aeronautics and Astronautics, Sun Yat-sen University, Guangzhou, China

<sup>c</sup> Key Laboratory of Geospatial Technology for the Middle and Lower Yellow River Regions, Ministry of Education, Henan University, Kaifeng, China

## ARTICLE INFO

Editor: Marie Weiss

### Keywords:

Night light  
VIIRS  
Anisotropy  
Radiance  
Radiant intensity

## ABSTRACT

Recent studies have described the anisotropy of ALAN based on statistical analysis of a quadratic model-based relationship between radiances derived from the VIIRS Day/Night Band sensor onboard Suomi-NPP and viewing zenith angle (VZA) (Li et al., 2019). Contrary to conventional wisdom, the satellite-observed radiance of ALAN always decreases at first and then increase with VZA, especially for high building areas. This leads to a so-called ‘cold-spot’ effect (i.e. radiance reaches local minimum in a specific VZA) in the VZA-radiance relationship, one that has not been understood using existing remote sensing methods. In this paper, we propose using radiant intensity – a measure of light power in a specific direction– to characterize the anisotropy of satellite-observed artificial lights at night (ALAN). Accordingly, we propose a new study design based on analysis across fourteen global cities. A linear regression model describing the relationship between VZA and radiant intensity resulted in an averaged regression  $R^2$  between 0.26 and 0.73 for the cities, suggesting a decay of radiant intensity with increased VZA. We then introduced a cosine-corrected linear model to describe the VZA-radiance relationship, which is mathematically transformed from the linear VZA-intensity model. Our results suggest that the ‘cold spot’ effect in the VZA-radiance relationship is consistent with the revealed phenomenon that the radiant intensity decays with increased VZA. We also constructed indexes related to urban morphology derived from LiDAR data, including the Blocking Index (BI), the Standard Deviation of Building Height (SDBH) and Average Building Height (ABH). These variables were all moderately or strongly correlated (Pearson correlation coefficient  $< -0.45$ ) to the Change Index (CI), which describes the anisotropic pattern of ALAN in the VZA-intensity relationship, in the four U.S. cities where LiDAR data is accessible. We conclude that radiant intensity is a suitable physical index to characterize the directional distribution of ALAN that can help understand the anisotropy of ALAN.

## 1. Introduction

In modern society, the electrified areas emit bright artificial light at night (ALAN), a symbol of economic and human activities (Levin et al., 2020). The Defense Meteorological Satellite Program/Operational Linescan System (DMSP/OLS), originally designed for meteorological observation, has been proven to record ALAN in cloud-free weather condition (Croft, 1978; Elvidge et al., 1997). The Earth Observation Group (EOG) has produced DMSP/OLS ALAN composites for more than two decades. These products have been widely applied in research fields of economics (Chen and Nordhaus, 2011; Henderson et al., 2011), urban extent mapping (Cao et al., 2009; Lu et al., 2008; Xie and Weng, 2016;

Zhou et al., 2014), urbanization (Liu et al., 2012; Small and Elvidge, 2013; Zhang and Seto, 2011), poverty (Elvidge et al., 2009), energy consumption (Sánchez de Miguel et al., 2013), fishery (Waluda et al., 2008), conflict (Li and Li, 2014) as well as light pollution (Bennie et al., 2015).

Since January 2012, the Suomi National Polar-Orbiting Partnership (Suomi NPP)’s Visible Infrared Imaging Radiometer Suite (VIIRS) has provided a new data source of nighttime light images (Elvidge et al., 2013). Comparing to DMSP/OLS images, the VIIRS images have higher spatial resolution and calibrated non-saturated radiometric values (Miller et al., 2013). Similar to DMSP/OLS, the VIIRS nighttime light images have also been utilized in different study domains (Kyba et al.,

\* Corresponding author.

E-mail address: [li\\_rs@163.com](mailto:li_rs@163.com) (X. Li).

2017; Levin, 2017; Levin et al., 2020; Li et al., 2013; Mann et al., 2016; Sharma et al., 2016; Yu et al., 2015). Another important advantage of VIIRS dataset is that the daily imagery are accessible to the public. The daily products are more sensitive to short term change of nighttime light, and therefore are able to capture effects of disasters (Cao et al., 2013; Zhao et al., 2018) and instability of electricity supply (Elvidge et al., 2020; Mann et al., 2016). Recently, NASA has provided a new nighttime light product for Suomi-NPP, named Black Marble (VNP46), at a daily, monthly, and annual temporal resolutions (Román et al., 2018). The Black Marble product suite has accounted for cloud, atmospheric, terrain, vegetation, snow, lunar and stray light effects. It is a data source that captures daily nighttime light dynamics, such as post-disaster response and long-term recovery (Román et al., 2019).

A recent study has revealed that the satellite-observed radiance of ALAN has strong anisotropic characteristic (Li et al., 2019), which has received increasing attention by scholars (Tong et al., 2020; Wang et al., 2021; Kyba et al., 2021a), and thus the Black Marble research group has created multi-angular monthly and annual night-time light product considering the anisotropy (Román et al., 2021). However, the revealed anisotropic patterns (e.g. cold effect) seem difficult to understand based on the existing literature. Accordingly, this study revisits the concepts of optical nighttime remote sensing quantities that can improve our ability to establish the anisotropy of ALAN. To do so, we use NASA's Black Marble product suite and introduce the term 'radiant intensity' – a measure of emitted light power in a specific direction. We then explore the potential factors that influence the anisotropy using radiant intensity.

## 2. Research motivation and hypothesis

### 2.1. The quadratic VZA-radiance model

During the 1980s, astronomers raised interest in the city emission function (CEF), which modeled the directional distribution of upward city light emission. It can help to understand the sky brightness, which is a kind of light pollution (Garstang, 1986). In recent decades, the CEF has been widely studied with ground-based observation and simulation methods (Cinzano and Castro, 1998; Luginbuhl et al., 2009; Kocifaj et al., 2015; Kocifaj and Lamphar, 2016; Kocifaj, 2018). In addition, scientists proposed that the remote sensing observation from above can play a role in studying the CEF and its related issues (Sánchez de Miguel et al., 2013; Coesfeld et al., 2018).

Related to CEF, anisotropy of artificial light at night, which describes the directional distribution of emitted light leaving the Earth's surface, has been investigated recently. However, these two terms are based on different physical units, lumen and watt, respectively.

For the anisotropy of artificial light at night, the relationship between satellite viewing zenith angle (VZA) and the nighttime radiance of VIIRS DNB was initially quantified by a quadratic model (Li et al., 2019):

$$\text{radiance} = a\text{VZA}^2 + b\text{VZA} + c \quad (1)$$

As Fig. 1 shows, the VZA and radiance have a quadratic relationship: as the VZA increases, the radiance decreases at first and returns after a certain degree which is defined as the 'cold spot'. Here,  $a$ ,  $b$  and  $c$  are the coefficients of the equation. Although the quadratic model sometimes does not fit the VZA-radiance relation very accurately (e.g. the radiance increases linearly when VZA is between 60° and 70° in some locations), it can generally describe the relation. It is also interesting that physiognomy, or morphology, may also impact the VZA-radiance relationship. For instance, urban areas with concentrated high building footprints tend to have clearer hot (i.e. radiance reaches a local maximum when VZA is zero) and cold spot (i.e. radiance reaches local minimum in a specific VZA) effects than predominantly low building areas, as illustrated in Fig. 1. Similarly, Tong et al. (2020) showed that the VZA-radiance relationship differs between suburban areas and downtown urban centers.

However, the pattern of the revealed anisotropy seems strange. For example, there is always a cold spot in the VZA-radiance relationship. Does the cold spot mean the satellite-observed light power reach the local minimum in a specific VZA? If yes, the current theory and conventional wisdom is difficult to explain the cold spot.

### 2.2. Research hypothesis

This study aims to investigate the meaning behind the quadratic VZA-radiance model, especially for the cold spot effect. For this purpose, we proposed two hypothesis and one assertion as follows.

**Hypothesis A.** The emitted power of satellite-observed ALAN has an approximately linear decay pattern as the VZA increases.

**Hypothesis testing:** Use radiant intensity as the metric to test the above hypothesized pattern, and we will name this pattern as linear VZA-intensity relationship.

**Hypothesis B.** The quadratic VZA-radiance relationship, including the cold spot effect, is approximately equivalent to the linear VZA-intensity relationship.

**Hypothesis testing:** Use mathematic inference, simulated data and real satellite data to test this hypothesis.

**Assertion A.** Use of radiant intensity can help to understand the anisotropy of ALAN and its relation to other factors.

**Assertion support:** Derive several urban morphological indexes from LiDAR data, and test their relationships to Change Index which is a key

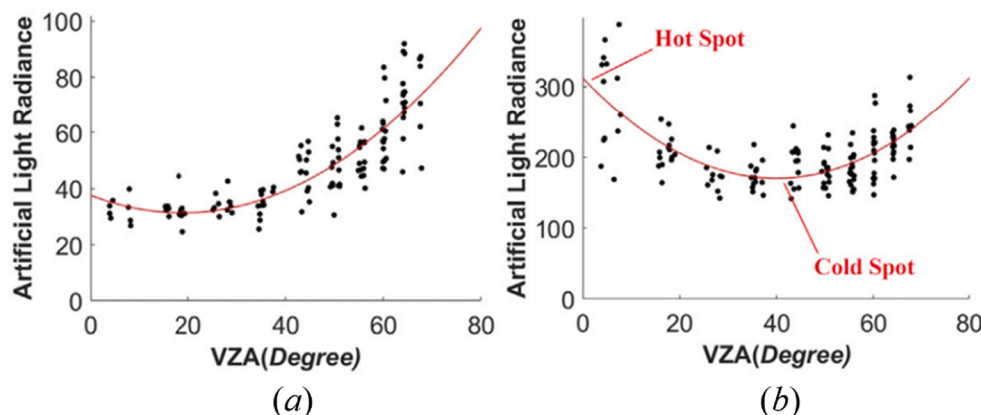


**Fig. 1.** Two examples of the relationship between viewing zenith angle and radiance ( $\text{nW}/\text{cm}^2/\text{sr}$ ): (a) A low building area in Houston (b) A high building area in Houston. This figure was extracted from the paper by Li et al. (2019).

parameter describing shape of the linear VZA-intensity relationship.

In rest of this paper, the two hypothesis will be tested, and the assertion will be evaluated. We note that our goal is not aimed at fully explaining all the mechanisms behind the anisotropy of ALAN. Instead, this paper focuses on using appropriate physical quantities (i.e., radiant intensity) to characterize the anisotropy of ALAN.

### 3. Study area and data

#### 3.1. Study area

The main study area include 14 global cities, which contain different urban forms and population size, and they are distributed over Europe, Middle East, USA and Asia. The characteristics of the study areas are summarized in Table 1, and Fig. 2 shows the study area of Los Angeles. In addition to these cities, the Queen District, New York City was used to analyze the impact of seasonality of environmental factors in Section 6.2.

#### 3.2. Study data

##### 3.2.1. Nighttime lights products

We chose NASA's Black Marble product suite (VNP46, Collection V001) as our primary data source of the ALAN images. NASA's Black Marble product suite includes daily at-sensor TOA nighttime radiances (VNP46A1) and daily moonlight adjusted NTL (VNP46A2), which are downloadable from NASA website (<https://ladsweb.modaps.eosdis.nasa.gov/>). The VNP46A2 product, with a spatial resolution of 0.004167 degree, was employed as the nighttime light data because the moonlight and atmospheric effects were removed (Román et al., 2018), and the ALAN was remained in the images.

**Table 1**  
The areas in this study. The population data is for the year around 2020 (<https://worldpopulationreview.com/world-cities>).

City	Population (million)	Study area center	VIIRS pixels	Year for VIIRS	Year for LiDAR
Atlanta, USA	0.52	33.768°N, 84.391°W	28 × 27	2019	2019
Bologna, Italy	0.80	44.495°N, 11.339°E	19 × 42	2013	No LiDAR data
Gaziantep, Turkey	1.73	37.068°N, 37.369°E	18 × 26	2016	No LiDAR data
Houston, USA	2.32	29.758°N, 95.406°W	60 × 68	2018	2018
Jerusalem, Israel/ Palestine	0.94	31.767°N, 35.205°E	17 × 22	2016	No LiDAR data
Los Angeles, USA	3.98	34.005°N, 118.229°W	49 × 86	2016	2015–2016
Las Vegas, USA	0.66	36.145°N, 115.181°W	33 × 44	2016	2016
Medina, Saudi Arabia	1.51	24.444°N, 39.601°E	32 × 54	2016	No LiDAR data
Paris, France	11.07	48.855°N, 2.372°E	39 × 52	2013	No LiDAR data
Rome, Italy	4.27	41.897°N, 12.496°E	42 × 60	2013	No LiDAR data
Samut Prakan, Thailand	1.32	13.544°N, 100.259°E	16 × 25	2016	No LiDAR data
Tianjin, China	13.79	39.121°N, 117.237°E	55 × 71	2016	No LiDAR data
Udon Thani, Thailand	0.57	17.392°N, 102.798°E	21 × 28	2016	No LiDAR data
Xuchang, China	1.00	34.033°N, 113.829°E	29 × 31	2016	No LiDAR data

#### 3.2.2. LiDAR data

In this study, we attempted to explore the relationship between the anisotropy of the ALAN and the urban morphology. The urban morphological data was derived from the LiDAR data provided by United States Geological Survey (USGS) (downloaded from <https://viewer.nationalmap.gov/basic/>). Among the total fourteen cities in this study, the LiDAR data is available for four U.S. cities, Atlanta, Houston, Los Angeles and Las Vegas. Using the LiDAR data, Digital Surface Model (DSM) without trees and the Digital Elevation Model (DEM) of the study area were generated by LiDAR 360 which is a software for processing 3D point cloud (<https://greenvalleyintl.com/software/lidar360/>). Finally, the DEM and DEM raster data at 4 m resolution were generated.

### 4. Methodology

#### 4.1. Definition of radiance and radiant intensity

First, it is necessary to review the measurement of the nighttime light product, including the Black Marble, which is radiance. The definition of radiance (<https://www.iso.org/standard/16943.html>) is as follows:

$$\text{radiance} = \frac{d\Phi}{d\Omega dA \cos \theta} \quad (2)$$

where  $\Omega$  is the solid angle,  $dA \cos \theta$  is the projected area in the viewing direction,  $\Phi$  is the radiant flux. In the VIIRS products including the Black Marble, the equation is rewritten as:

$$\text{radiance} = \frac{dP}{d\Omega^* S \cos VZA} \quad (3)$$

where  $P$  is the power emitted from the pixel (we used “pixel” short for ground area corresponding to the pixel),  $\Omega$  is the solid angle, and  $S$  is the pixel size and VZA is the viewing zenith angle.

In addition to radiance, radiant intensity is an important variable to measure the emitted light power in a specific direction, the radiant intensity is defined as:

$$\text{intensity} = \frac{dP}{d\Omega} \quad (4)$$

From the definition, radiant intensity can directly reflect emitted light power in a specific direction, while radiance refers to the observed brightness because the projected area is involved. Following the Eqs. (3)–(4), we derive that

$$\text{intensity} = \text{radiance} * S \cos VZA \quad (5)$$

From the definitions, radiant intensity is the only variable that can describe the angular distribution of the emitted power of ALAN. Thus, given a scenario that radiance of a pixel is increased when VZA is larger, it is correct to say the pixel is brighter but incorrect to say the pixel emits more upward light power when VZA is larger. Similarly, in astronomical light pollution studies, the directional distribution of upward ALAN has been characterized by the luminous intensity, traditionally defined as luminous flux per solid angle (Cinzano and Castro, 1998; Luginbuhl et al., 2009; Kocifaj et al., 2015; Kocifaj and Lamphar, 2016; Kocifaj, 2018), which is analogous to radiant intensity.

#### 4.2. VIIRS data preprocessing

The purpose of this section is to prepare the data of artificial light at night (ALAN) and viewing zenith angle (VZA). For every pixel in the study area, we extracted the radiance from the VNP46A2 product, while satellite zenith angle (VZA), satellite azimuth angle (VAA) and solar zenith angle (SZA) values were extracted from the corresponding VNP46A1 product. To remove the influence of solar illumination, pixels with SZA less than 108° were excluded. In addition, we also labeled the

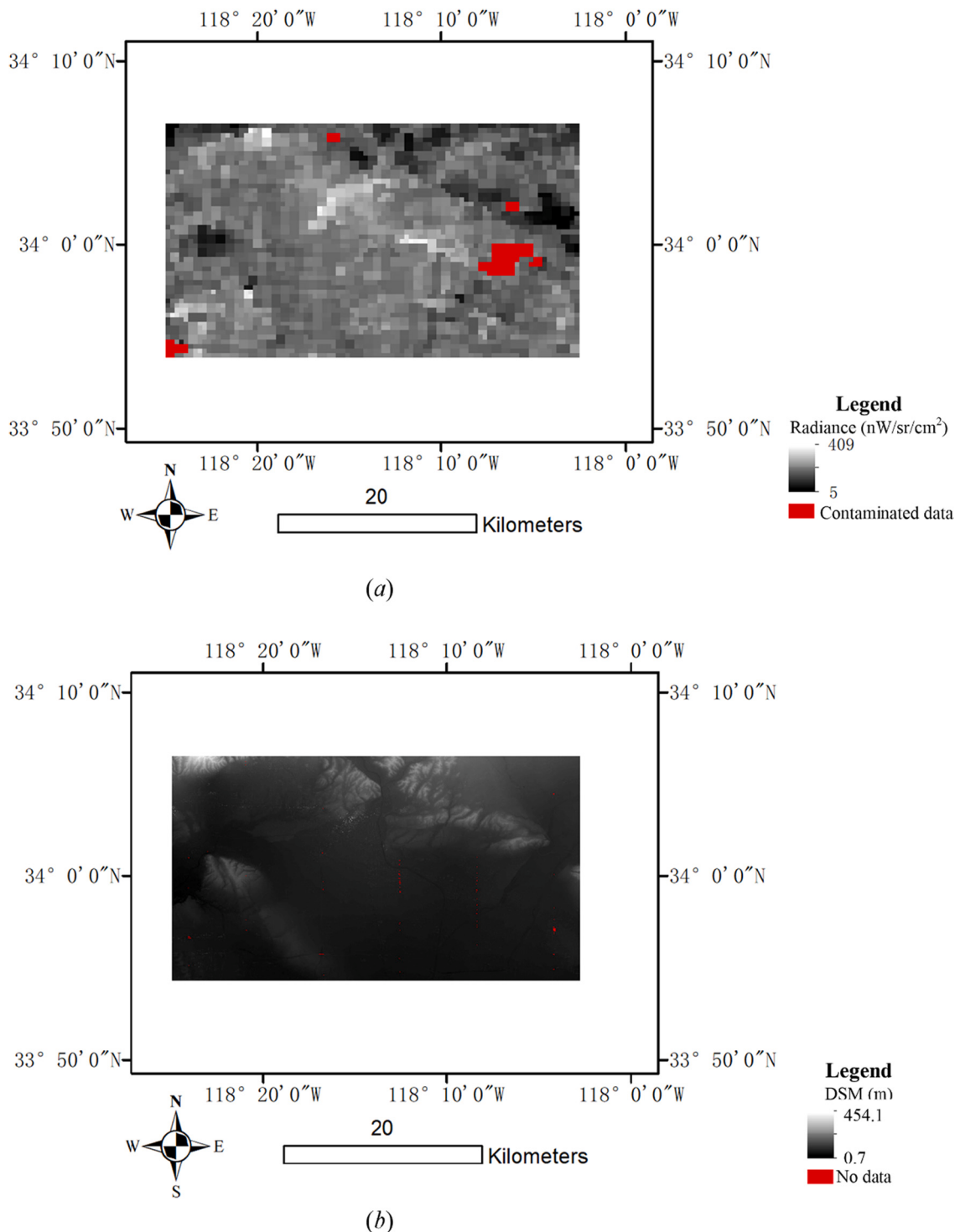


**Fig. 2.** The study area of Los Angeles: (a) Black Marble nighttime lights acquired in Jan 1, 2016; (b) Digital Surface Model (DSM) derived from LiDAR.

cloud-contaminated pixels based on the Mandatory Quality Flag band available in the VNP46A2 product.

To alleviate the geometric mismatch among time series Black Marble NTL retrievals (Román et al., 2018), a  $3 \times 3$  pixel window is used to calculate the average radiance inside the window, and the angle information (e.g. VZA and VAA) from the central pixel is viewed as the information for the window. Each window generated a sample, including radiance and VZA data for the whole study period.

#### 4.3. Modelling VZA-intensity relation

To test Hypothesis A, both the linear and quadratic models were used to quantify the VZA-intensity relationship as follows:

$$\text{intensity} = a\text{VZA} + b \quad (6)$$

$$\text{intensity} = a\text{VZA}^2 + b\text{VZA} + c \quad (7)$$

where intensity denotes radiant intensity in the above equations and in

the rest of this paper. For regression of each sample, we got the coefficients,  $R^2$  and  $p$ -value.

Through the analysis, which will be presented in [Section 5.1](#), we will view linear regression as a proper model (Eq. [\(6\)](#)) to describe the VZA-intensity relationship. To quantify change of radiant intensity with the change of VZA, a Change Index (CI) for the radiant intensity is constructed as follows:

$$\text{CI} = \frac{a}{b} \quad (8)$$

The unit of CI, in the Eq. [\(8\)](#), is 1/degree.  $a$  and  $b$  are the coefficients in which the radiant intensity is linearly correlated to the VZA.

#### 4.4. Transforming linear VZA-intensity model

Since the radiant intensity can be approximately modeled by linear regression from VZA (Eq. [\(6\)](#)), which will be proved in [Section 5.1](#). Combining Eq. [\(5\)](#) and [\(6\)](#), radiance can thus be modeled as follows:

$$\text{radiance} = \frac{a\text{VZA} + b}{Scos\text{VZA}} \quad (9)$$

Considering the pixel size  $S$  is a constant when the pixel is fixed, the model can be rewritten to a cosine-corrected linear VZA-radiance model:

$$\text{radiance} = \frac{c\text{VZA} + d}{cos\text{VZA}} \quad (10)$$

To test [Hypothesis B](#), we will compare the cosine-corrected linear VZA-radiance model to the quadratic model using simulated and real satellite data.

#### 4.5. Analyzing the impact of urban morphology on the anisotropy

To demonstrate the usefulness of radiant intensity and evaluate [Assertion A](#), we will generate several urban factors and analyze their relationship to the Change Index.

##### 4.5.1. Geometric index

We hypothesized that the urban morphology impacts the Change Index (CI). Therefore, we construct a blocking index for any target point on the ground to measure the urban morphology. Given a target point, in the direction represented by azimuth angle  $\phi$ , there is a maximal elevation angle that can see the building, denoted by  $\beta_\phi$ , as illustrated in [Fig. 3](#). Therefore,  $\beta_\phi$  ranges from  $-90$  to  $90^\circ$ , with a larger value representing a target point that is more occluded (e.g., when the target point is on the top of a building,  $\beta_\phi$  is negative). The  $\beta_\phi$  is calculated based the Digital Surface Model (DSM) derived from the USGS LiDAR data as described in [Section 3.2.2](#). To search the DSM data around the

target point for calculation of  $\beta_\phi$ , a search radius is necessary, and we set it to 1 km in this study.

Considering the Suomi NPP satellite has limited azimuth viewing angles (VAA) for a target point on the ground, we constructed a Blocking Index (BI) for the target point:

$$\text{BI} = \sum_{\phi \in X} \frac{\beta_\phi}{n} \quad (11)$$

The blocking Index (BI) represents the averaged blocking effect when satellite views one location with different VAAs. In Eq. [\(11\)](#),  $X$  denotes all the satellite VAAs for the target point, and  $n$  denotes the number of elements inside  $X$ . However, since our study's spatial extent in each city is limited, the azimuth range is almost the same in the same city. For convenience, the VAA elements in  $X$  are set to integers. This study only considers the blocking effect on the street light. Therefore, only the BI on the ground is viewed as valid BI. The ground is defined as the difference between DEM and DSM is less than 1 m in our analysis. Thus, in this analysis, valid values of BI are between 0 and  $90^\circ$ .

The process to calculate the BI for a VNP46 retrieval is summarized as follows: 1) generate a ground mask where  $|DSM - DEM| < 1$  m for the study area; 2) for any pixel in the DSM, a circle centered at this pixel with radius of 1 km is used to calculate the BI index of this pixel as illustrated in [Fig. 4 \(a\) and \(c\)](#); 3) if any area of this circle is out of the spatial extent of the DSM, the corresponding point is discarded for analysis; 4) for each VNP46 pixel, record the number of valid BI pixels that fall into the VNP46 pixel, and only the VNP46 pixels, with no less than 95% of the area having corresponding BI, were regarded as valid VNP46 pixels (the no-data BI pixels exist because DSM has some no-data area); 5) for the valid VNP46 pixels, calculate the averaged BI index for the ground part (see example in [Fig. 4\(d\)](#)) inside the  $3 \times 3$  VNP46 pixel, and it is used as the BI for the VNP46 image.

##### 4.5.2. Statistical index

In addition to the constructed geometric index, we also constructed two statistical indexes. Firstly, the average building height (ABH) in a specific region is calculated as:

$$\text{ABH} = \sum_{i=1}^n \frac{h_i}{n} \quad (12)$$

where  $h_i$  is the height for  $i$ th location, which is calculated as:

$$h_i = DSM_i - DEM_i \quad (13)$$

where  $DSM_i$  and  $DEM_i$  are the DSM and DEM values for the  $i$ th location in the region. An example is given in [Fig. 4 \(b\)](#).

Secondly, the standard deviation of the building height (SDBH) in

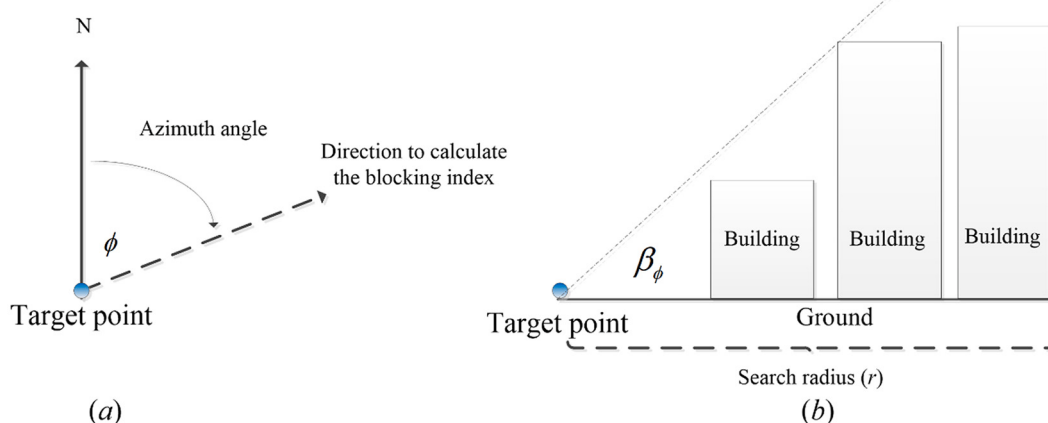


**Fig. 3.** Schematic diagram of the blocking Index: (a) schematic diagram of the azimuth; (b) definition of  $\beta_\phi$ .

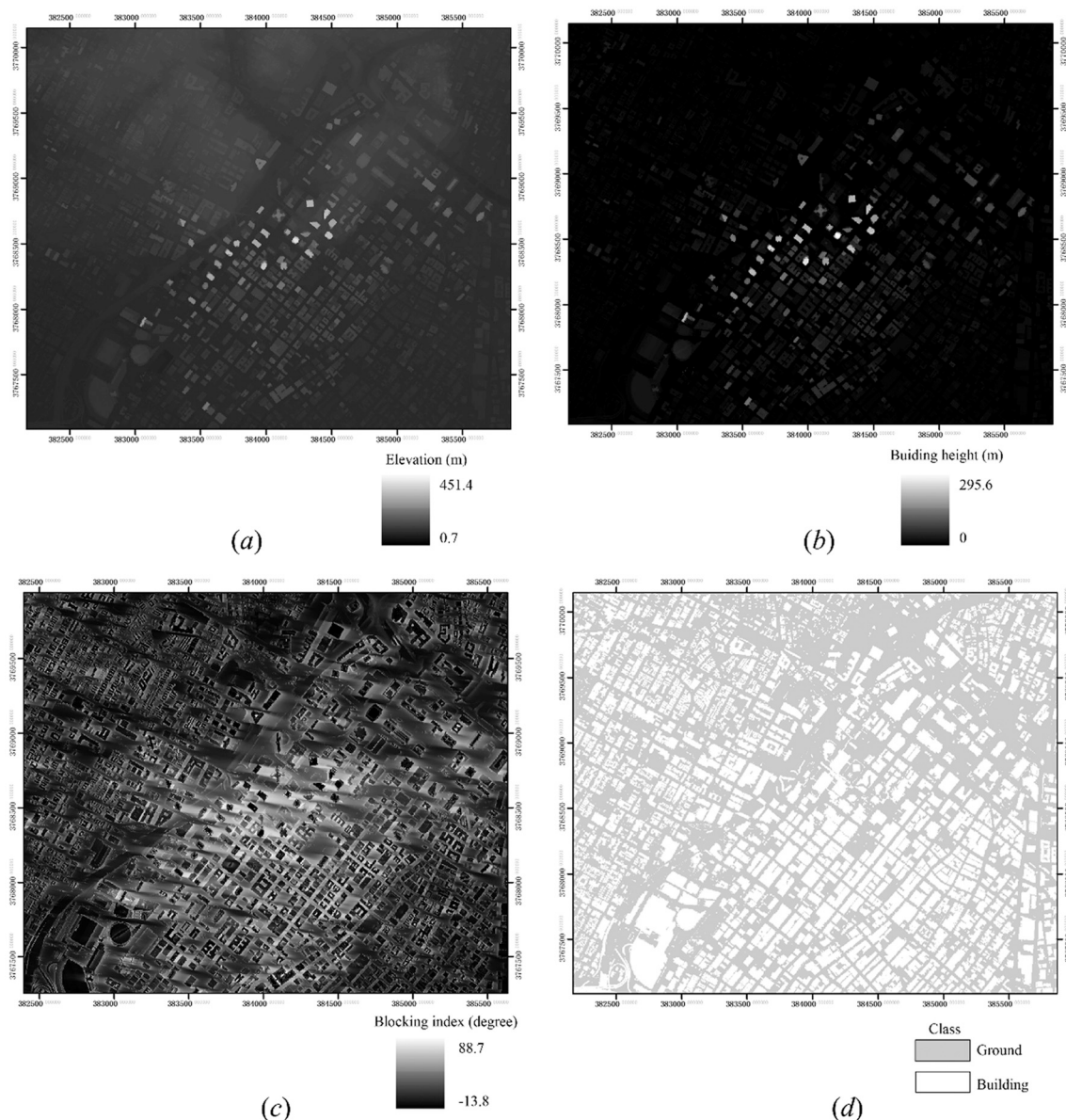


**Fig. 4.** A sub-image of the DSM in Los Angeles and its derived variables: (a) the DSM; (b) the building height; (c) Blocking Index; (d) Class (ground or building). Coordinate System: UTM, Zone 11 North.

the region is defined as:

$$\text{SDBH} = \sqrt{\sum_{i=1}^n \frac{(h_i - \text{ABH})^2}{n-1}} \quad (14)$$

The SDBH represents the building height variation in a region, which potentially impacts the anisotropy but needs tests in further steps. The SDBH for each  $3 \times 3$  VNP46 pixel window was calculated based on Eq. (14).

#### 4.5.3. Impact analysis

The above sections have proposed three indexes (BI, ABH and SDBH) as potential impact factors on the anisotropy, which is measured by the Change Index (CI) from Eq. (8). We will analyze the relationship between each index and CI by using correlation analysis.

## 5. Result and analysis

### 5.1. VZA-intensity relation

The VZA-intensity relationship can show the directional distribution of satellite-observed power of ALAN, and also to test [Hypothesis A](#). As introduced in [Section 4.2](#), the radiance and VZA data were derived from the moving window on the time series VNP46 retrievals to generate study samples. As an example, [Fig. 5](#) shows the VZA-radiance relationship and VZA-intensity relationship of two samples in Los Angeles and Houston. Although the VZA-radiance has different patterns, its trend is similar to a quadratic function curve described by Eq. (1), which has been revealed by the previous study ([Li et al., 2019](#)).

We used linear and quadratic models, from Eqs. (6)–(7), to model the VZA-intensity relationship for all the samples. [Table 2](#) summarized the regression results of 14 cities. The quadratic model and linear model have very close  $R^2$  for different cities. Also, the variation of the  $R^2$  of the two models are very close for each city, with the standard deviation of  $R^2$  of the quadratic model slightly higher than that of the linear model. For

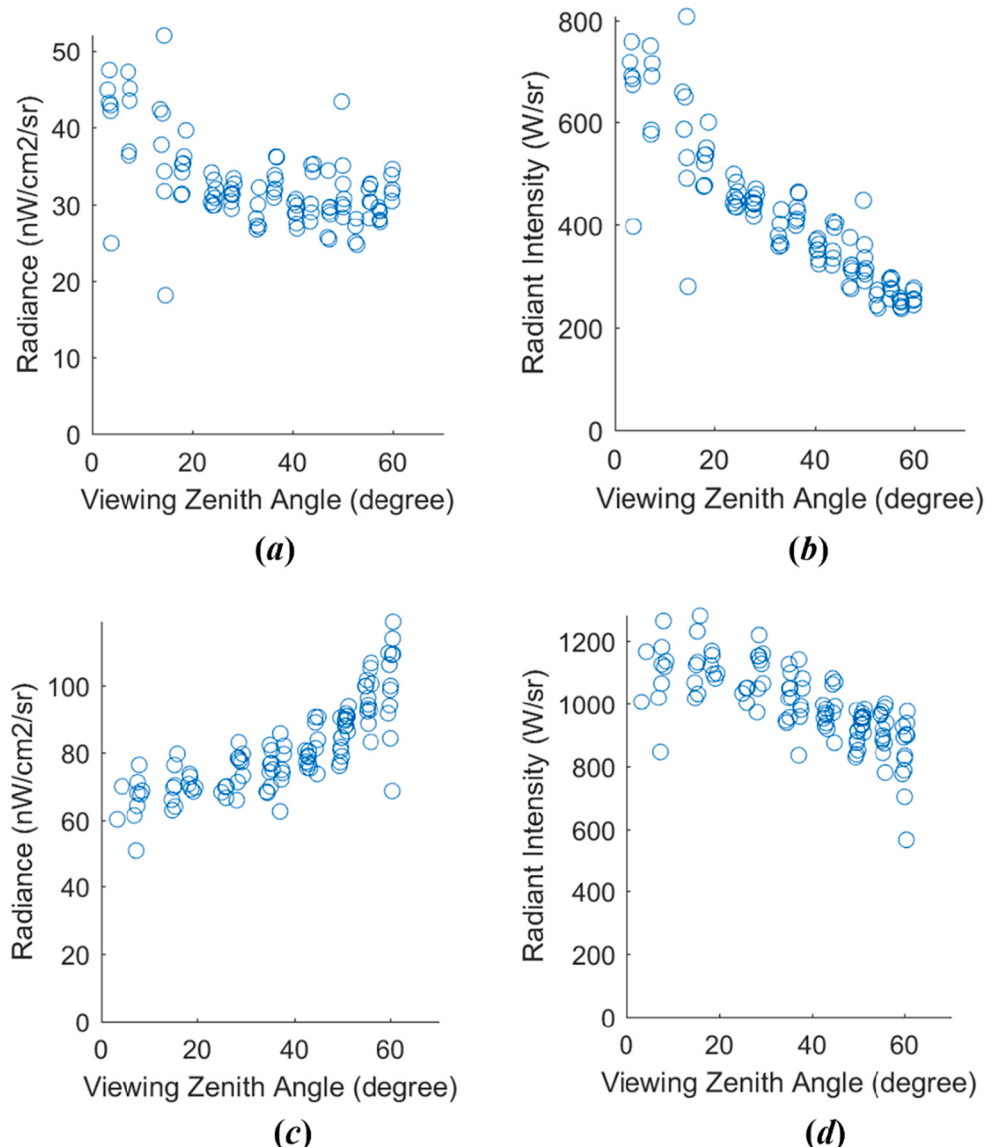


**Fig. 5.** The relationship between VZA and two variables (radiance and radiant intensity) in two locations: (a) VZA versus radiance in 34.104°N 118.400°W (Los Angeles); (b) VZA versus radiant intensity in 34.104°N 118.400°W (Los Angeles); (c) VZA versus radiance in 29.788°N 95.288°W (Houston); (d) VZA versus radiant intensity in 29.788°N 95.288°W (Houston).

example, in Los Angeles, there are 3948 samples for analysis. The linear and quadratic VZA-intensity models resulted in  $R^2$  of 0.4511 and 0.4750, respectively, showing that the performance linear model is close to the quadratic model. For the linear VZA-intensity model in Los Angeles, there are 3887 samples having significant results, among which 100% of the samples have negative values of  $a$  and CI. For all samples in all the cities,  $a$  and CI values are negative when the linear regression is significant ( $p < 0.01$ ). The averaged CI for different cities is between  $-0.00839$  and  $-0.00534$ . In addition, the average values of the coefficients,  $a$  and  $b$ , in the linear model, were listed in the table.

In addition, we also randomly selected 20 locations with different land use or urban forms as examples to show the different of the two models (Table 3). For these samples, the two model performances are also very close, with only one location (the 17th sample) that has  $R^2$  difference larger than 0.05.

It is informative to explore the  $R^2$  difference linked to the urban surface. Here, we show some locations inside the 14 cities where the model  $R^2$  difference between the linear and quadratic models is larger than 0.15 (there are very few locations at this value), and we found that

these geographic locations include residential regions and commercial regions (Fig. 6), and there seem not clear pattern in which the locations are distributed. However, it seems that the “pure residential” regions do not have the pattern that  $R^2$  difference is very large, while the residential regions of Fig. 6 (a) (b) are mixed with large commercial regions (shopping center) and stadium.

All the above findings indicate that, for most of the areas, the satellite-observed power from ALAN approximately follows a linear decay pattern when the VZA is larger. Therefore, Hypothesis A has been supported.

## 5.2. From linear VZA-intensity model to quadratic VZA-radiance model

This section is to test Hypothesis B.

### 5.2.1. Analysis using simulated data

Since the relationship between VZA and radiant intensity can be modeled by a linear regression model as revealed in Section 5.1. We used the cosine-corrected linear model (Eq. (10)) to model the VZA-radiance

**Table 2**

The regression for VZA and radiant intensity over 14 global cities. The number of samples is equal to  $(m-2)(n-2)$ , where  $m$  and  $n$  are the size of the VNP46A2 image patch, because the moving window for the sample has  $3 \times 3$  pixels. Note: A/L and A/Q represent average  $R^2$  for the linear and quadratic models, respectively, and S/L and S/Q represents standard deviation of the  $R^2$  for the linear and quadratic model, respectively.

City	Samples	Statistics of $R^2$ in the two models				Samples with significant linear regression	Ratio of negative CIs in significant linear regression (%)	Average index in significant linear regression					
		A/L		S/L				A/Q		S/Q			
		A/L	S/L	A/Q	S/Q			A/L	S/L	A/Q	S/Q		
Atlanta	650	0.5864	0.1037	0.6112	0.1037	650	100	-0.00796	-13.36	1420.52			
Bologna	680	0.4350	0.1961	0.4711	0.2063	644	100	-0.00669	-3.46	504.95			
Gaziantep	384	0.7379	0.1090	0.7634	0.1092	384	100	-0.00839	-9.40	1095.08			
Houston	3828	0.5022	0.2022	0.5187	0.2031	3737	100	-0.00589	-6.81	1034.17			
Jerusalem	300	0.6989	0.1611	0.7184	0.1618	300	100	-0.00764	-13.18	1641.20			
Los Angeles	3948	0.4511	0.1734	0.4750	0.1740	3887	100	-0.00534	-6.07	981.30			
Las Vegas	1302	0.4800	0.1374	0.5057	0.1324	1302	100	-0.00670	-22.19	2215.15			
Medina	1560	0.5084	0.2248	0.5343	0.2335	1508	100	-0.00719	-13.66	1811.39			
Paris	1850	0.3329	0.1316	0.3659	0.1316	1813	100	-0.00699	-8.21	1091.33			
Rome	2320	0.5827	0.2152	0.6076	0.2181	2250	100	-0.00774	-7.50	894.10			
SamutPrakan	322	0.4068	0.1896	0.4355	0.1964	289	100	-0.00566	-1.86	309.51			
Tianjin	3657	0.2617	0.1451	0.2925	0.1523	3288	100	-0.00638	-3.65	521.47			
UdonThani	494	0.3892	0.1773	0.4034	0.1793	475	100	-0.00659	-1.55	218.71			
Xuchang	783	0.3121	0.1810	0.3452	0.1916	679	100	-0.00649	-1.34	185.95			

**Table 3**

The 20 selected points and its modelling result for the two VZA-intensity models. Note: City/High and City/Low represent high and low building areas in cities, respectively.

NO.	Country	Geography /Land use	Longitude	Latitude	R <sup>2</sup> for VZA-intensity relation	
					Linear	Quadratic
1	Saudi Arabia	City/High	39.602°E	24.469°N	0.4659	0.4823
2	France	City/High	2.244°E	48.890°N	0.4694	0.4734
3	USA	City/High	118.256°W	34.052°N	0.7729	0.7931
4	USA	City/High	115.173°W	36.115°N	0.6843	0.7028
5	Thailand	City/Low	102.798°E	17.398°N	0.3824	0.4131
6	Turkey	City/Low	32.823°E	39.877°N	0.8584	0.8707
7	Italy	City/Low	12.510°E	41.919°N	0.8758	0.8831
8	USA	City/Low	115.106°W	36.190°N	0.2435	0.2790
9	USA	City/Low	118.302°W	33.965°N	0.5125	0.5463
10	France	Industry	5.952°E	49.502°N	0.2571	0.2967
11	China	Industry	117.223°E	39.215°N	0.2267	0.2480
12	USA	Industry	84.619°W	35.898°N	0.0796	0.0800
13	Turkey	Industry	37.410°E	37.094°N	0.5739	0.5900
14	Saudi Arabia	Rural	39.831°E	24.581°N	0.3037	0.3080
15	Italy	Rural	12.552°E	41.735°N	0.3749	0.4191
16	Turkey	Rural	35.273°E	36.919°N	0.4003	0.4027
17	Thailand	Rural	100.860°E	13.952°N	0.3463	0.4248
18	USA	Rural	83.965°W	33.294°N	0.3649	0.3729
19	China	Rural	118.598°E	36.660°N	0.0369	0.0371
20	USA	Rural	115.515°W	33.123°N	0.3118	0.3195

relationship, as proposed in Section 4.4.

We will use numerical analysis to compare these two models. To observe the shape of the cosine-corrected linear VZA-radiance curve, different values of  $c$  are used while  $d$  is fixed to  $100\text{nW/cm}^2/\text{sr}$  ( $d$  can be viewed as a scaling factor), and the curves are drawn in Fig. 7.

All these curves, derived from the cosine-corrected linear VZA-radiance model, are similar to the quadratic model from visual interpretation, as illustrated in Fig. 7. To quantitatively analyze the consistency between the two models, we changed  $c/d$  from  $-0.0001/\text{degree}$  to  $-0.01/\text{degree}$  with an interval of  $0.0001/\text{degree}$  by fixing  $d$  to  $100\text{nW/cm}^2/\text{sr}$ , and a data set of the VZA and radiance were generated using Eq. (10). Consequently, we use the quadratic VZA-radiance model to fit the generated VZA and radiance data and get the values of model  $R^2$ . For all the  $c/d$  values, the model  $R^2$  is larger than 0.95. This simulation result proves that the linear decay of radiant intensity is very close to the quadratic VZA-radiance pattern.

Furthermore, we use the cosine-corrected linear VZA-radiance model to analyze the relationship between the cold spot angle and the CI. For each value of  $c/d$  (Change Index), we get the VZA value corresponding to the minimal radiance and recorded this VZA value as the cold spot angle.

Then a curve describing the relation between Change Index (CI) and the cold spot angle is generated in Fig. 8. This curve shows that the cold spot angle moves from small to large with the decrease of the CI. In other words, the cold spot angle is larger when the radiant intensity decays faster.

### 5.2.2. Analysis using satellite data

The above analysis suggests the cosine-corrected linear model is highly consistent to the quadratic model by analyzing the simulated data. Here, in addition, the real VNP46A2 data is used to compare the two models. For each sample, including VZA and radiance values, the cosine-corrected linear VZA-radiance model and the quadratic model were used to fit them, and the model  $R^2$  was calculated for each sample. Thereby, the average model  $R^2$  was calculated for each city as shown in Fig. 9. It shows that the quadratic model has a slightly higher  $R^2$  than the cosine-corrected linear model, and the largest  $R^2$  difference is only 0.0334. Considering that the cosine-corrected linear regression only has two coefficients compared to the three coefficients of the quadratic model, we can conclude that the cosine-corrected linear model is close to the quadratic model when modelling the VZA-radiance relation.

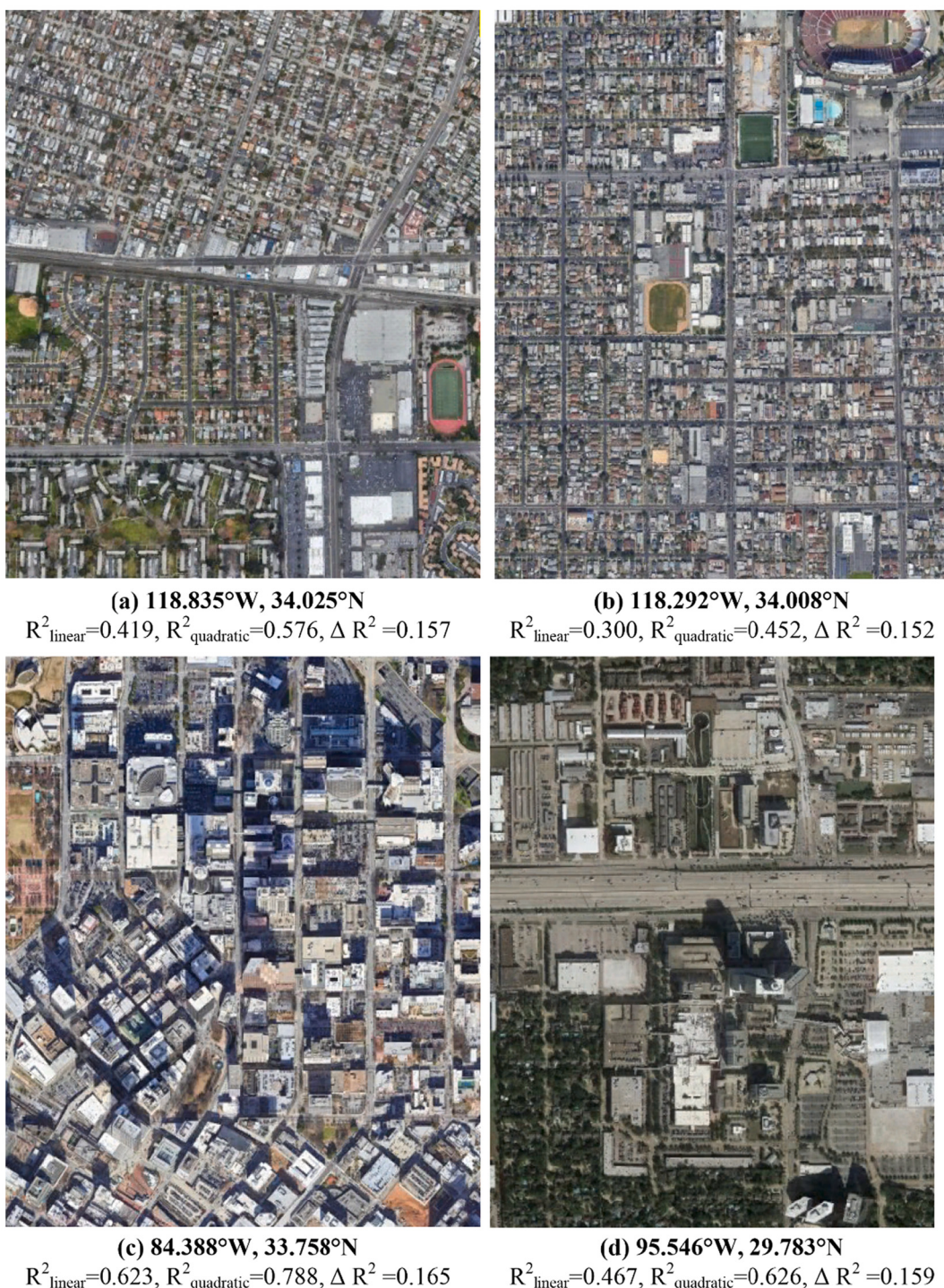


**Fig. 6.** Selected areas with large  $R^2$  difference between the linear and quadratic models.

Based on the simulated data analysis and real satellite data analysis, we can conclude that the cosine-corrected linear VZA-radiance model is approximately equivalent to the quadratic VZA-radiance model. Thus, **Hypothesis B** has been proved.

### 5.3. Relation between urban morphology and the anisotropy

As the Change Index (CI) can directly reflect how the satellite-observed power of ALAN decay with the increase of VZA, if we analyze the relationship between CI and some environmental factors, it is possible to see how the factors impact CI. If these impacts accord with

conventional wisdom, we can say the radiant intensity has advantages in measuring the anisotropy of ALAN so that **Assertion A** can be supported.

Specifically, we hypothesized that the urban buildings block more street light in a larger viewing zenith angle (VZA). To test this hypothesis, we used the indexes which describe the urban morphology and test their relation to the anisotropy of ALAN using Pearson correlation analysis. For analysis in each city, we defined valid sample as the samples with less than 5% of original BI values (i.e. the BI at the resolution of DSM) missed and significant in the linear VZA-intensity regression ( $p < 0.01$ ), and only valid samples are finally used for this correlation analysis.

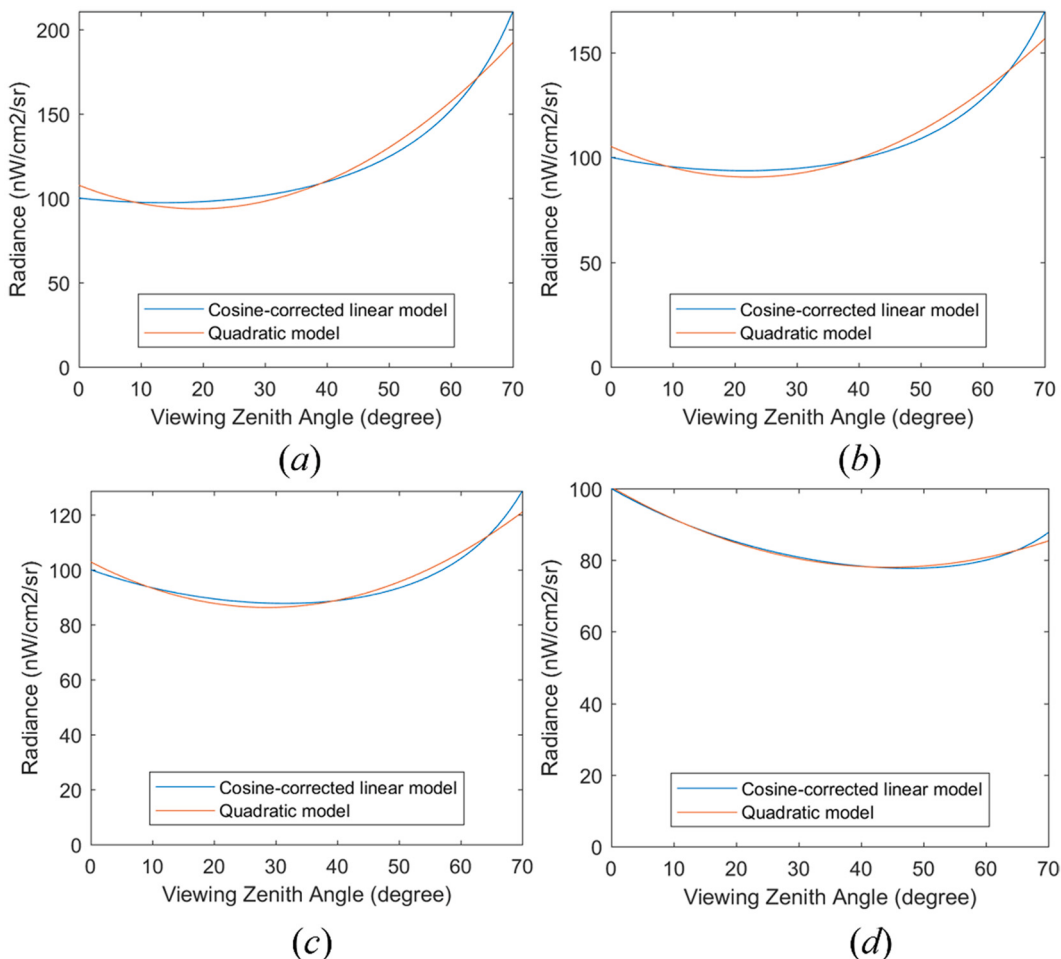


**Fig. 7.** The VZA-radiance curve derived from the cosine-corrected linear VZA-radiance model and the fitted curve using quadratic regression by setting  $d = 100$ : (a)  $c = -0.4$ ; (b)  $c = -0.6$ ; (c)  $c = -0.8$ ; (d)  $c = -1$ . The units of  $d$  and  $c$  are  $\text{nW}/\text{cm}^2/\text{sr}$  and  $\text{nW}/\text{cm}^2/\text{sr}/\text{degree}$ , respectively.

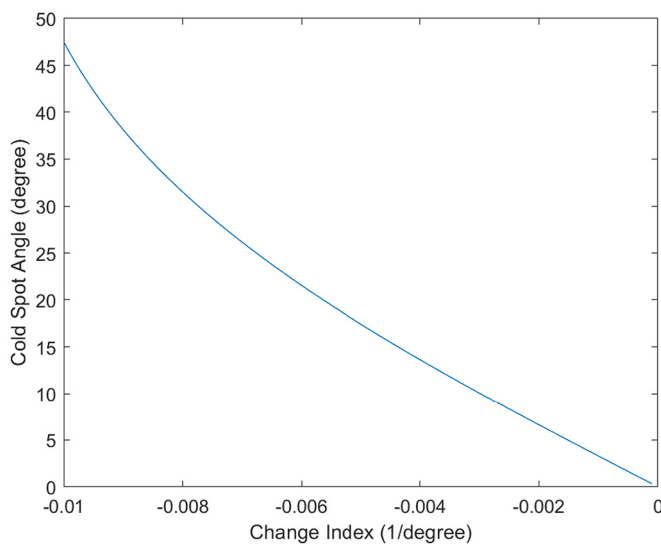


**Fig. 8.** The relationship between the Change Index and cold spot angle from the simulated data

**Fig. 10** shows the Change Index is significantly correlated to the three indexes in the four cities ( $p < 0.01$ ). The scatterplots illustrated that Blocking Index (BI), Standard Deviation of the Building Height

(SDBH) and Average Building Height (ABH) are all negatively correlated to the Change Index (CI). In other words, a stronger blocking effect and more variation of urban building height may result in faster decay of the emitted light power when the VZA becomes larger.

The above analysis shows that the correlation between CI and the three indexes are moderate, and some high values of the indexes may enlarge the correlation. For example, the correlation between ABH and CI may decrease if the points with extremely high values of ABH are removed. To evaluate the impact of extreme high values on the regression, we removed samples with top high values of each index, and used the rest of the data set for regression. **Table 4** shows the result from the data selection strategy with 5% of highest values removed. The results suggest that the extremely high values of the indexes in the upper tails have an important impact on the regression – the relations are much weaker by removing the high values. However, they still stay significant ( $p < 0.01$ ). In sum, the urban morphology has substantial impacts on the anisotropy of ALAN even if some extreme samples were removed.

The previous study finds a cold spot, which is the local minimum, in the VZA-radiance curve. One important feature to characterize the cold spot is the angular value of the cold spot. We also previously found that the cold spot angle for the high building area was larger than that of the low building area (Li et al., 2019). Combining the negative correlation between CI and cold spot angle (Fig. 8) and the negative correlation between CI and the average building height (Fig. 10), average building height (ABH) would be positively correlated to the cold spot angle. **Fig. 11** shows the relation between ABH and cold spot angle, which was estimated from the axis of symmetry of the quadratic model (Note: the

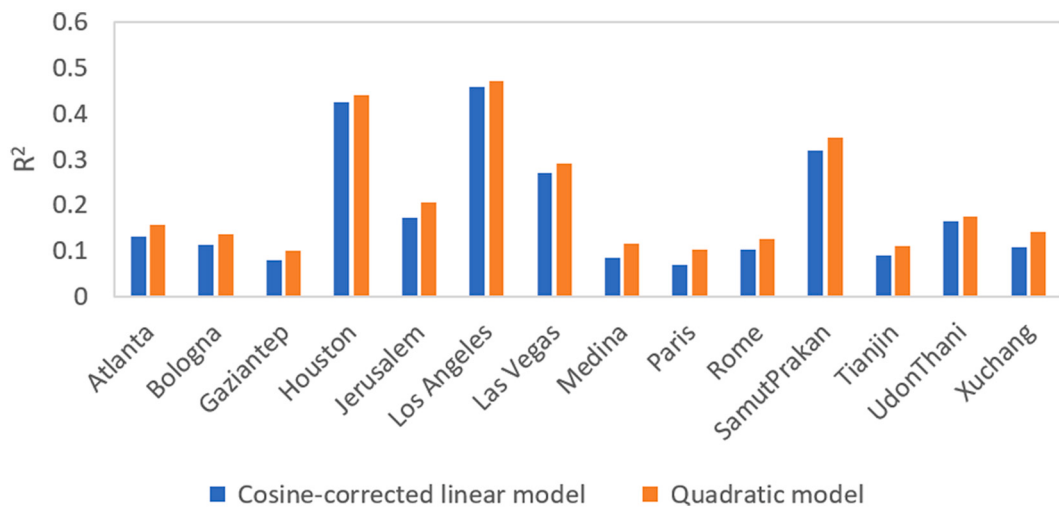


Fig. 9. The averaged  $R^2$  of the two models for the VZA-radiance relation

angle may be less than 0 degree or larger than 70 degree because the symmetry may be out of the VZA range). We found that the correlations are all significant ( $p < 0.01$ ) and the coefficients are 0.5125, 0.5131, 0.4664 and 0.6822, for Los Angeles, Houston, Atlanta and Las Vegas, respectively, suggesting areas with higher buildings tend to have larger cold spot angle. Although this relation is significant, the points with high ABH values may have large impact on the regression. We remove the samples with high ABH values and test the updated correlation as shown in Table 5. It is interesting that the correlation is still significant and positive even if the ABH range is limited to  $4 \text{ m} \geq \text{ABH} \geq 0$  for the four cities. In addition, we also test the correlation when ABH is very high (e.g.  $\text{ABH} \geq 10 \text{ m}$ ), finding out that it is significant only for Los Angeles ( $p < 0.05$ ). In summary, the cold spot angle tends to be larger in higher building areas, but in very high building areas (e.g.  $\text{ABH} > 10 \text{ m}$ ), this correlation is not significant.

## 6. Discussion

### 6.1. Robust regression between VZA and radiant intensity

The regression analysis between VZA and radiant intensity shows that the two variables are only correlated at moderate level, which is probably derived from uncertainty of VNP46A2 data processing such as atmospheric correction and night-to-night change of the ALAN. At a lower performance, this correlation is perhaps partly caused by the outliers. We hypothesize that the calculation of Change Index (CI) can be improved as these uncertainties from the outliers can be alleviated, so that the correlation analysis performance between CI and the three indexes may be enhanced.

For this purpose, we used a robust regression technique (Rousseeuw and Leroy, 2005), an iterative procedure to minimize the impact of outliers on the coefficient estimation. In robust regression, the weight function determines the scale factor that influences the points of different residuals on the regression coefficients. The tuning constant, which downweights the contribution of outliers, is an important parameter in the robust regression (Rousseeuw and Leroy, 2005). In this study, the robust regression was implemented by using the *robustfit* function in the Matlab. We chose the ‘welsch’ as the weight function, we used different values (e.g., from 0.5 to 30) of the tuning constant to the robust regression model and calculated the CI value corresponding to each tuning constant. ‘welsch’ is a weight function that the weight of a point in the sample is proportional to the exponential function of negative residual sum of squares. Next, we calculated the Pearson correlation coefficients between CI and three indexes (BI, SDBH and ABH) to evaluate if the robust regression can improve the relationship

between the CI and the indexes. Finally, we selected the largest absolute value of the correlation coefficient from different tuning constants to represent the best performance of the robust regression.

Table 6 gives the Pearson coefficients between the CI and different indexes. In addition, the table also lists the coefficients based on the ordinary linear regression in the last row. It shows that the relationship between CI and the three indexes has nearly no improvement. This analysis suggests that the impact of outliers (VZA and radiant intensity) on the CI is not important.

### 6.2. Evaluation of the seasonal impact

A previous study by Levin (2017) showed that satellite-observed nighttime light reoccurring changes due to the seasonality, including surface albedo, vegetation phenology, and snow cover. Therefore, assuming that the VZA dynamic is related to these seasonal variations, the real mechanism behind the VZA-radiance (or VZA-intensity) relation may be the VZA-seasonality relation. In other words, if the VZA changes with the NDVI in time series, the VZA-radiance (VZA-intensity) relationship is directly influenced by these additional factors.

To test the above hypothesis, we choose three regions for analysis. The first two regions are the studied Los Angeles and Houston, the third region in the Queen District, New York City with VNP46A data in year of 2015. The third region is centered at  $73.825^\circ\text{W}$   $40.715^\circ\text{N}$ , and there are  $23 \times 56$  VNP46A2 pixels for analysis, and the average  $R^2$  for the linear VZA-intensity regression model is 0.2537, suggesting that the anisotropy also exists in this region.

We choose three locations from the three regions, respectively, and show the time series VZA, NDVI (MOD13A1.006) and albedo (White-sky albedo for visible broadband in MCD43A3.006) in Fig. 12. Snow cover data is not presented as it can be reflected in the albedo dynamics. The time series of three variables show that the VZA is irrelevant to NDVI or albedo from visual comparison because VZA has a much shorter change period. Moreover, we used correlation analysis to analyze the relation between VZA and the other two variables. We found that, for all the samples from the three regions, there is no sample that VZA is significantly ( $p < 0.05$ ) correlated to NDVI or albedo. This result suggests that the relationship between VZA and radiance (or radiant intensity) is not derived from the impact of seasonal environmental factors on the satellite-observed ALAN.

### 6.3. Model $R^2$ for the linear VZA-intensity relationship

Table 2 shows that the averaged  $R^2$  values for the linear VZA-intensity model are very different in different cities, with the largest

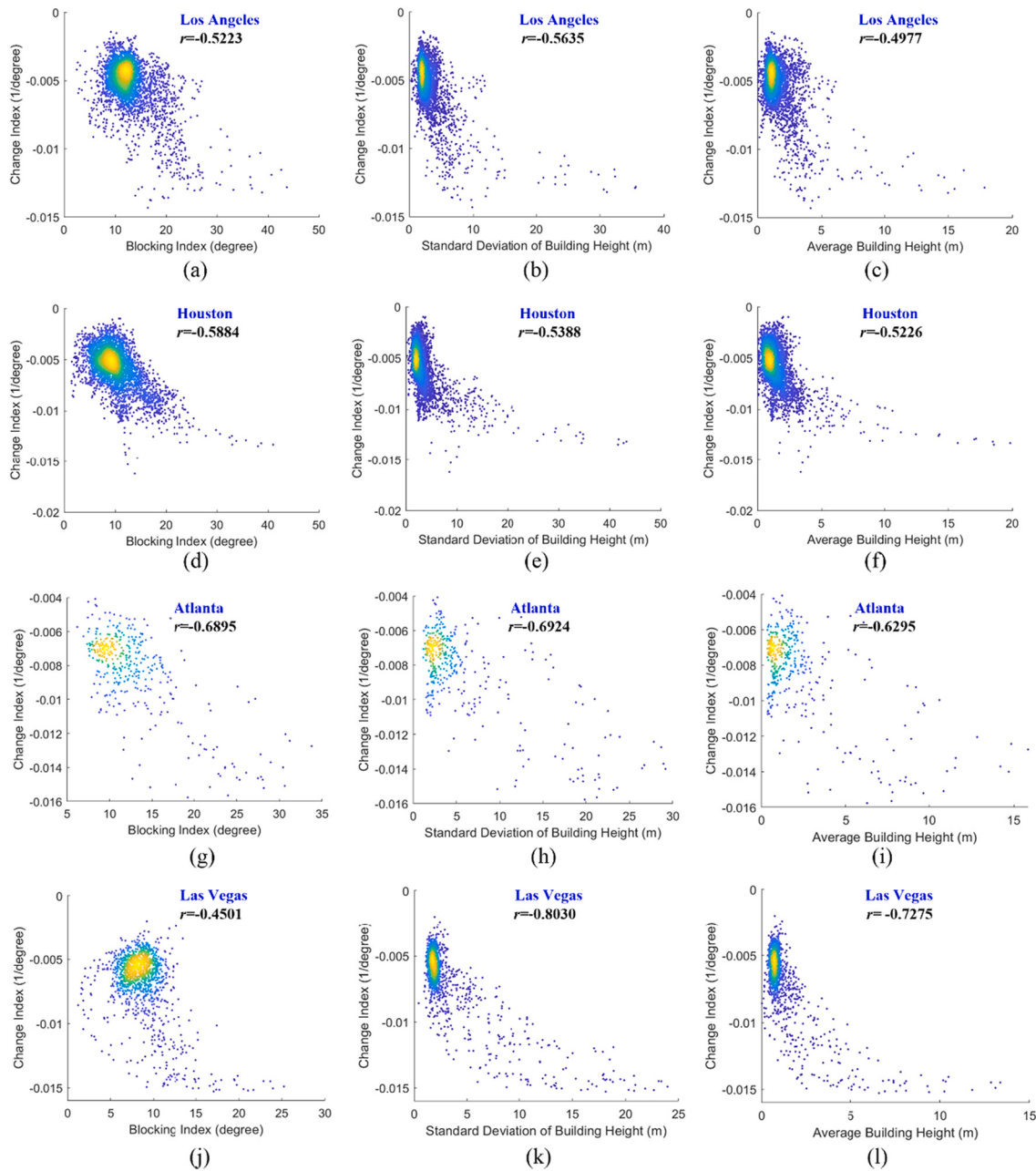


**Fig. 10.** Scatterplot and the Pearson correlation coefficient of variable pairs: (a) BI versus CI in Los Angeles; (b) SDBH versus CI in Los Angeles; (c) ABH versus CI in Los Angeles; (d) BI versus CI in Houston; (e) SDBH versus CI in Houston; (f) ABH versus CI in Houston; (g) BI versus CI in Atlanta; (h) SDBH versus CI in Atlanta; (i) ABH versus CI in Atlanta; (j) BI versus CI in Las Vegas; (k) SDBH versus CI in Las Vegas; (l) ABH versus CI in Las Vegas

**Table 4**

The Pearson correlation coefficient between Change Index (CI) and three indexes (BI, SDBH, ABH). 100% data represents that no data was discarded, 95% data means the samples with highest 5% of the index values were discarded. All the correlation coefficients are significant ( $p < 0.01$ ).

City	Index	Correlation coefficient		City	Index	Correlation coefficient	
		100% data <sup>a</sup>	95% data			100% data	95% data
Los Angeles	BI	-0.5223	-0.2979	Atlanta	BI	-0.6895	-0.4576
	SDBH	-0.5635	-0.4226		SDBH	-0.6924	-0.4530
	ABH	-0.4977	-0.3163		ABH	-0.6295	-0.3718
Houston	BI	-0.5884	-0.4548	Las Vegas	BI	-0.4501	-0.1176
	SDBH	-0.5388	-0.4410		SDBH	-0.8030	-0.6939
	ABH	-0.5226	-0.3947		ABH	-0.7275	-0.5916

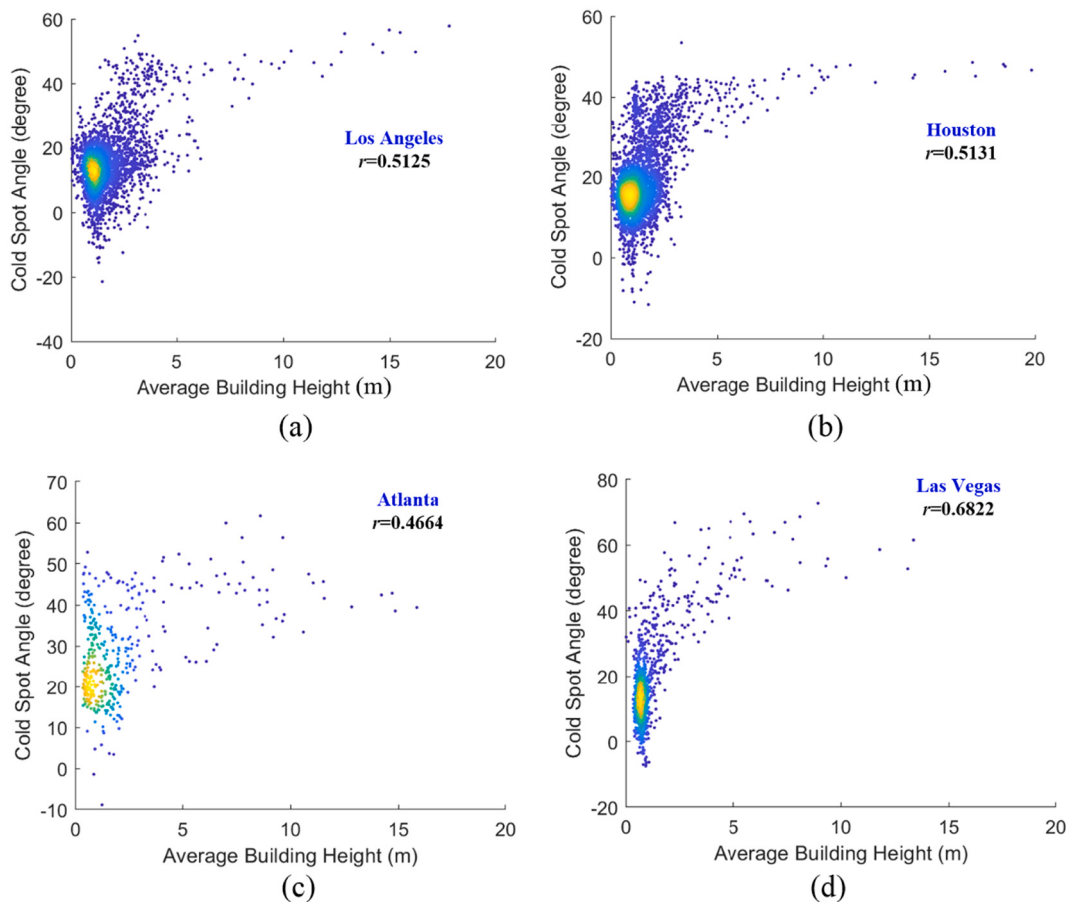


**Fig. 11.** The relationship between average building height (ABH) and cold spot angle: (a) Los Angeles; (b) Houston; (c) Atlanta; (d) Las Vegas

**Table 5**

Pearson correlation coefficient between ABH and cold spot angle with different ranges of ABH. ‘max’ denotes the maximal ABH value for each city.

City	Range of ABH (m)					
	[0, max]	[0, 10]	[0, 8]	[0, 6]	[0, 4]	[10, max]
Los Angeles	0.5125**	0.4726**	0.4537**	0.4305**	0.3674**	0.6754*
Houston	0.5131**	0.5314**	0.5215**	0.5065**	0.4448**	0.4198
Atlanta	0.4664**	0.4672**	0.4217**	0.3062**	0.1787**	-0.2044
Las Vegas	0.6822**	0.7074**	0.7041**	0.7008**	0.6281**	0.6223

\*\* Significant  $p < 0.01$ .

\* Significant  $p < 0.05$ .

**Table 6**

The correlation between the CI and the three indexes (BI, SDBH and ABH).

Weight function in the robust regression	Pearson Correlation Coefficient					
	Robust regression			Ordinary regression		
	BI	SDBH	ABH	BI	SDBH	ABH
Los Angeles	-0.5257	-0.5633	-0.4997	-0.5223	-0.5635	-0.4977
Houston	-0.5940	-0.5378	-0.5208	-0.5884	-0.5388	-0.5226
Atlanta	-0.6891	-0.6920	-0.6289	-0.6895	-0.6924	-0.6295
Las Vegas	-0.4595	-0.8094	-0.7426	-0.4501	-0.8030	-0.7275

value of 0.7379 and the lowest value of 0.2617, thus it is interesting to explore the potential factors behind this large difference. Since most of the VZA-intensity samples can be modeled by the linear model, we hypothesize that there are two major factors determining the model  $R^2$ . Firstly, uncertainty of the night light observations would make model  $R^2$  lower. The uncertainty is appeared as the one-to-many relationship (e.g.

very close VZA values have corresponding radiant intensity or radiance values with large gap) as shown in Figs. 1 and 5. Thus, the model  $R^2$  value is smaller when the uncertainty is larger. Secondly, the change trend of radiant intensity in the VZA-intensity relation would be another important factor. Larger change rate of the radiant intensity in the VZA-intensity relation would suppress the uncertainty effect when modelling

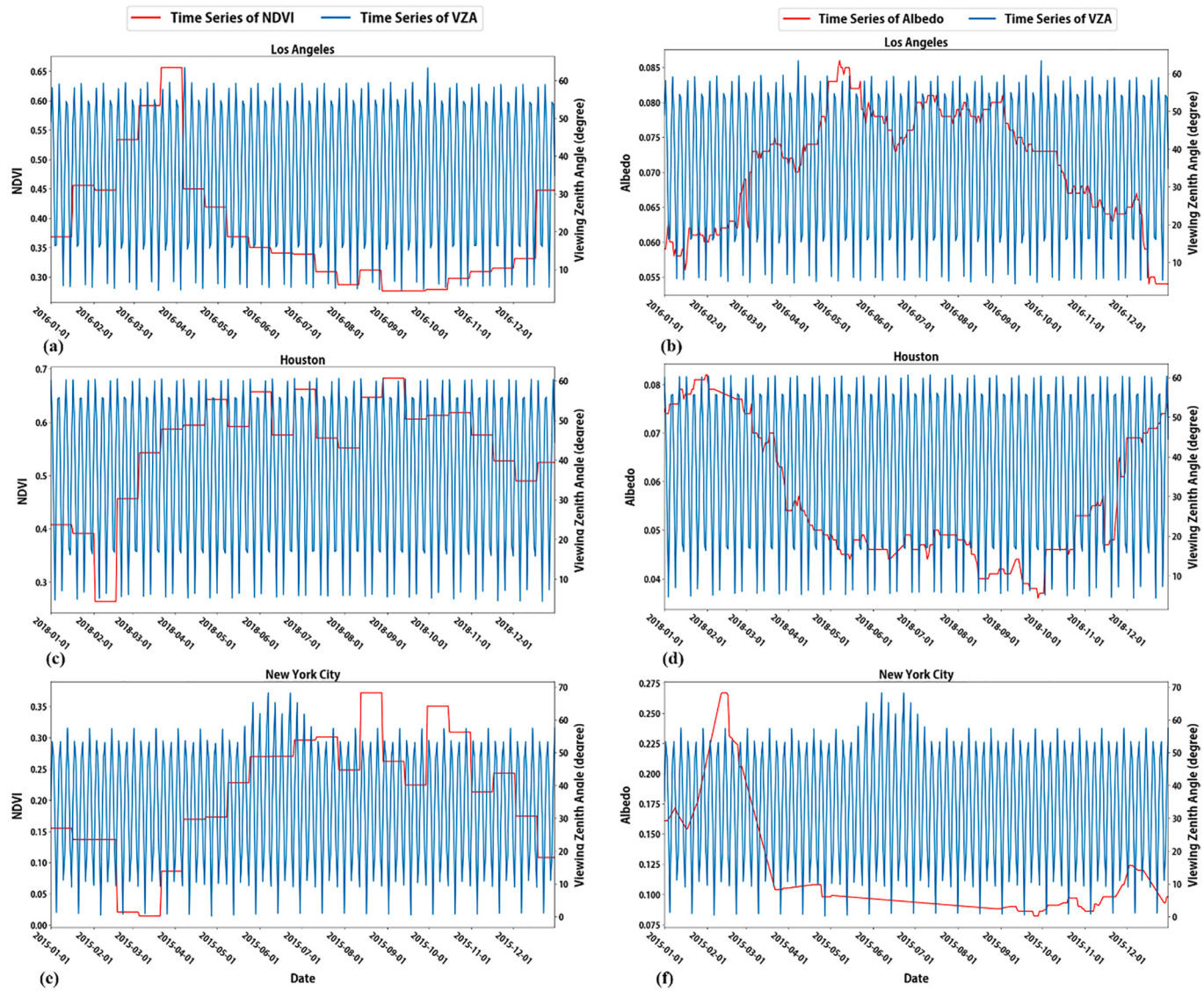


**Fig. 12.** The comparison of VZA and environmental factors: (a) VZA versus NDVI in Los Angeles ( $34.097^{\circ}\text{N}$   $118.193^{\circ}\text{W}$ ); (b) VZA versus albedo in Los Angeles ( $34.097^{\circ}\text{N}$   $118.193^{\circ}\text{W}$ ); (c) VZA versus NDVI in Houston ( $29.877^{\circ}\text{N}$   $95.439^{\circ}\text{W}$ ); (d) VZA versus albedo in Houston ( $29.877^{\circ}\text{N}$   $95.439^{\circ}\text{W}$ ); (e) VZA versus NDVI in New York City ( $73.885^{\circ}\text{N}$   $40.760^{\circ}\text{W}$ ); (f) VZA versus albedo in New York City ( $73.885^{\circ}\text{N}$   $40.760^{\circ}\text{W}$ ).

the VZA-intensity relation. Therefore, stronger change trend in the linear regression would enlarge the model  $R^2$ .

For the first aspect, we propose to build a Comprehensive Coefficient of Variation (CCV) to model the data uncertainty in the VZA-intensity model. Traditionally, the coefficient of variance (CV) has been used to measure the data uncertainty, which is calculated as the ratio of standard deviation to the average of the data. However, CV cannot be directly applied to describe the one-to-many VZA-intensity relation, because VZAs are not fixed in several values but are distributed around limited values as shown in Figs. 1 and 5. Therefore, we used a small moving window, including a small range the VZA values and their corresponding radiant intensity values, to calculate the uncertainty of radiant intensity by combining the uncertainty in all windows. Thus, the CCV is defined as:

$$\text{CCV} = \frac{\sum_{i=1}^n m_i \sigma_i}{\sum_{i=1}^n m_i \mu_i} \quad (15)$$

where  $m_i$  denotes the sample size in the  $i$ th moving window,  $n$  denotes

number of moving windows, and  $\sigma_i$  and  $\mu_i$  denote the standard deviation and mean value of the radiant intensity values, respectively, in the  $i$ th moving window. The VZA range (from approximately 0 to 60 degree) is equally divided into 20 intervals, and an interval (approximately 3 degrees) is defined as a valid interval where the sample size is no less than five and the linear VZA-intensity relation is not significant ( $p > 0.05$ ). The significant test is designed to avoid variation of radiant intensity which is caused by the VZA variation, because we aim to quantify the uncertainty of radiant intensity itself but not the VZA-derived radiant intensity change.

We used the Change Index (CI) to quantify the change trend of radiant intensity in the VZA-intensity relation. We used all valid samples over fourteen cities by removing the invalid samples with insignificant linear VZA-intensity regression because the Change Index is not meaningful in these cases. As result, we got 21,206 samples with their linear VZA-intensity model  $R^2$  (LVMR), CI and CCV. In addition, we calculated the average LVMR, CI and CCV of each city. Their relations are shown in Fig. 13, and we also used a linear model to predict LVMR from CI and CCV (Table 7).

Fig. 13 shows that both CI and CCV are moderately correlated to

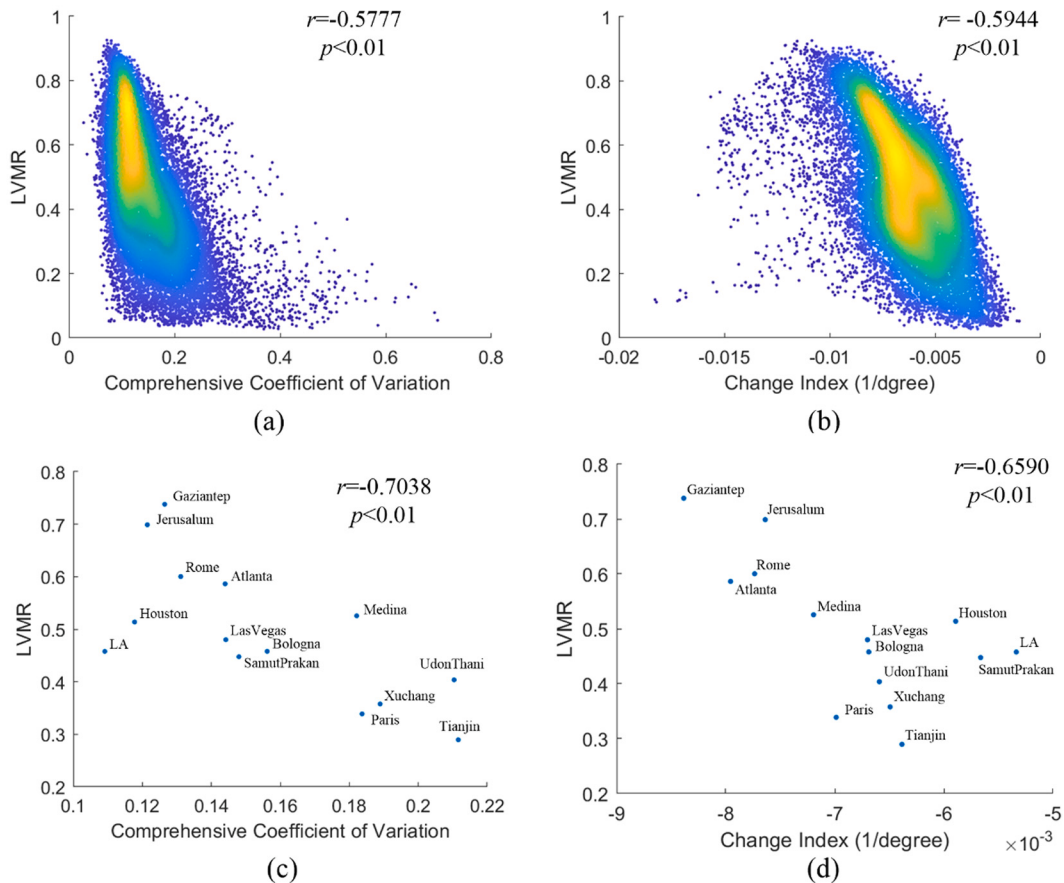


**Fig. 13.** Comprehensive Coefficient of Variation (CCV) and Change Index (CI) versus the linear VZA-intensity model  $R^2$  (LVMR): (a) CCV versus LVMR for all the locations; (b) CI versus LVMR for all the locations; (c) averaged CCV versus averaged LVMR for the 14 cities; (d) averaged CI versus averaged LVMR for all the 14 cities.

**Table 7**

Regression result of modelling LVMR from CI and CCV.

Sample set	Cities	Locations
$R^2$	0.868	0.846
Adjusted $R^2$	0.844	0.846
Number of Observations	14	21,206
Standardized coefficients		
CI	-0.660***	-0.728***
CCV	-0.612***	-0.714***

\*\*\* Significant under  $p < 0.001$ .

LVMR in both location and city level, with Pearson correlation coefficients of  $-0.5777$  and  $-0.5944$  for locations, and Pearson correlation coefficients of  $-0.7038$  and  $-0.6590$  for the city level. Table 7 shows that CI and CCV together can explain 84.6% and 84.4% of the variation of the LVMR for the locations and cities, respectively. More specifically, the standardized coefficients of two variables are very close for each sample set (i.e. locations and cities). The correlation and regression results suggest that the night light data uncertainty and the change trend of the radiant intensity in the VZA-intensity relation approximately equally contribute to the variation of the linear VZA-intensity model  $R^2$  for different locations and cities.

The mechanism behind the uncertainty is complicated and caused by many factors, including atmospheric correction errors, environmental seasonal factors such as ground albedo (Wang et al., 2021) and actual night-to-night change of city light. In comparison, the radiant intensity change trend is likely to be influenced by urban factors such as urban morphology (e.g. Fig. 10), building reflectivity, light emission type and spatial distribution of lights, which will be further discussed in Section

#### 6.4.

##### 6.4. Limitations, future work and implication

This study has two major parts. The first part is analyzing the relationship between VZA and radiant intensity. The averaged model  $R^2$  for the regression, including the linear and quadratic, is between 0.26 and 0.76 for each city, indicating that a unique VZA regime has various corresponding values of radiant intensity and radiance. This ‘one-to-many’ relationship has hindered accurate modelling of the multi-angular characteristics of satellite-derived ALAN values. First, The Aerosol Optical Depth (AOD 0.550  $\mu\text{m}$ ) for atmospheric correction of the current Black Marble product is extrapolated from daytime AOD since currently no nighttime AOD product is available (Román et al., 2018; Wang et al., 2021). The difference of daytime and nighttime AOD would increase the retrieval uncertainty in particular at large cities where temporal AOD variation is usually high (Filonchyk et al., 2019). Secondly, one of our assumptions of using the VNP46 time series is that the ALAN does not change from night to night. In fact, at least some major events, including human activities during holidays (Román and Stokes, 2015) result in abrupt short-term changes. Thirdly, one VZA retrieval has two corresponding viewing azimuth angles (VAAs) (Li et al., 2019), suggesting that the VAA may also contribute to the one-to-many relationship for VZA and radiant intensity. Fourthly, the satellite-observed ALAN has some seasonality which has already been reported by Levin et al., (2017), and it contributes to the ‘one-to-many’ relationship.

The second major part of this study is analyzing the possible impact of urban morphology on the VZA-intensity relationship measured by the Change Index (CI). Our results should be strictly interpreted within an

experimental assessment of how the VZA-intensity relationship is impacted by urban morphology. This is crucial since we only used three simple indexes as independent variables for our correlation analysis. It is also possible to explain the complicated VZA-intensity as well as the VZA-radiance relationship (e.g. the ABH-CI or ABH-cold-spot pattern is significant different when ABH changes from low to high values) by considering the following aspects: 1) urban morphology is much more complicated than the three indexes can model; 2) the reflectivity of buildings may also impact the Change Index (e.g., when a building's profile with low reflectance may be different from the building profile installed with glass curtain wall), and it implies that higher reflectance of building profile results in slower decay of ALAN on the side view angle; 3) given multiple light bounces exist between light sources and buildings, more interactions between lights and urban buildings should be accounted to better explain the anisotropy, while ray tracing method would be a choice; 4) the spatial distribution of ground light sources (e.g. the proposed Blocking Index, assumes that the ground light sources are equally distributed in different locations) as well as the shape of the street light emission (e.g. the shield on a street light will influence the emission direction) may also impact the modelling outputs; 5) Importantly, the proposed Blocking Index only considers the light from the ground while the light from building profiles may also contribute to the emitted light. Although these sources may not be a major component of ALAN in the overpass time of VIIRS DNB, the light's proportion is not negligible, which needs comprehensive investigation (Kyba et al., 2021b). Combining all the above aspects, we argue that a physical model needs to be developed to explain how different factors determine the anisotropy of satellite-observed ALAN, although such a model is very challenging.

The VIIRS sensor may be another factor influencing the revealed anisotropy in this paper. VIIRS combined use of segmented detectors and Ground Instantaneous Field of View (GIFOV) rotation to keep a uniform cross-track spatial resolution (Wolfe et al., 2013). This introduces a processing step that may derive a function of VZA. How this potential effect along with the urban morphology impacts the anisotropy is the issue which needs more elaborate efforts with ground observations to separate the effects of these two factors.

The analysis in Section 6.2 shows that the VZA-radiance (or radiant intensity) is not derived from the relationship between VZA and the seasonal environmental factors. This finding does not exclude the impact of the environmental factors on the anisotropy. For example, in leaf-off and leaf-on periods, the angular distribution of ALAN may be different as the obstacle of leafs on the upward light may change the angular distribution compared to the leaf-off scenario (Román et al., 2018). Investigating this issue may need data describing the phenology of trees such as the very high resolution images from National Agriculture Imagery Program of the US (<http://www.fsa.usda.gov/programs-and-services/aerial-photography/imagery-programs/naip-imager/>). Undoubtedly, this effect needs elaborate and comprehensive investigation over cities in different geography with considerable work in future.

In this paper, only four US cities (e.g. Los Angeles, Houston, Atlanta and Las Vegas) were included to analyze the relationship between the anisotropy and urban morphology, while cities in developing countries have different urban morphology which may derive some different findings to some extent. This limitation exists due to lacking of free and open LiDAR data from these countries, while the LiDAR data is the source for generating DEM, DSM and urban morphological indexes in our study. Thus, future work will include cities in developing countries once the LiDAR data is available.

Our previous work indicates that the unmanned aerial vehicles (UAVs) are capable of monitoring ALAN with multiple viewing angles as the atmospheric effect is minor for UAV observation, and nighttime light can be viewed as stable during UAV observation compared to that of the satellite observation (Li et al., 2020). However, multi-angular UAV observation on ALAN is also challenging (Li et al., 2020). For example, it

is difficult to keep all the locations in the images with the same observation angles as the flight height of UAV is very low. However, with development of future UAV techniques, we posit that multi-angular observation of ALAN by UAV would be more feasible.

In addition to clarifying some theoretical issues of the anisotropy, this study also gives implications for future applications. Firstly, this study will enrich the toolbox for modelling the City Emission Function (CEF) in light pollution research community. The CEF describes directional distribution of upward city light emission, measured by luminous intensity, and it helps to understand how city light impacts the skyglow (Cinzano and Castro, 1998; Luginbuhl et al., 2009; Kocifaj et al., 2015; Kocifaj and Lamphar, 2016; Kocifaj, 2018), while ground-based observation used to be the conventional way to model CEF in the community. Our study shows that satellite data can help to model the relation between VZA and radiant intensity, which is analogous to luminous intensity. Thus, our study implies that introducing satellite images, which is a cheaper and larger-covered data source than the ground-observation data, would be a contribution to modelling CEF in future studies. Secondly, our study will help to estimate the city light emission from the ground more accurately. Understanding how city light interacts with environmental factors is important to estimate the actual night-time light emission. For example, a previous study revealed that the seasonal change of ground albedo, vegetation and snow cover are determinants on the seasonal change of night-time light signal received by the satellite (Levin, 2017), thereby the actual night-time light emission can be better estimated if these seasonal factors are considered. Similarly, in this study we found that night-time light measured by radiant intensity has quantitative relation to the urban morphology, indicating that the satellite-observed night-time light emission is able to be corrected if the urban morphology is considered.

## 7. Conclusion

Recently, the anisotropy of satellite-derived artificial light at night (ALAN) has been revealed and quantified by using a quadratic VZA-radiance model (Li et al., 2019). The quadratic pattern, especially the cold spot effect (i.e. nighttime radiance decreases at first and then return with VZA increase), may be misinterpreted as that satellite-observed power of ALAN decreases at first and then return with the increase of VZA. In this study, based on physical nomenclature of nighttime remote sensing quantities, we argue that radiant intensity (instead of radiance), is the correct physical metric to measure the directional distribution of satellite-observed power of ALAN. To prove the usefulness of radiant intensity, we proposed two hypothesis and one assertion and developed null tests.

Using a linear regression model and data from 14 global cities, we found that the emitted power from ALAN approximately linearly decays when the viewing zenith angle (VZA) increases, which has not been reported in remote sensing community. Thus, Hypothesis A has been proved. This revealed phenomenon is also consistent to conventional wisdom, because occlusion of ALAN (i.e., blocking effect) would be stronger when the viewing zenith angle is larger. The linear VZA-intensity is then converted to the cosine-corrected VZA-radiance model, which is very close to the quadratic model, suggesting that the real phenomenon behind the quadratic VZA-radiance model, including the cold spot effect, is the approximately linear decay of satellite-observed power of ALAN. Thus, Hypothesis B has been proved as well. Based on the linear VZA-intensity model, we can infer new insights, e.g., how the blocking effect is related to the VZA-intensity relationship. Thus, Assertion A has been supported. The latter is also consistent with previous theories and findings (Sánchez de Miguel et al., 2013).

We conclude that radiant intensity is an efficient and useful physical metric when exploring the anisotropy of satellite-observed ALAN. Clarifying nomenclature and physical definition is the basic step for quantitative remote sensing as there were much misunderstanding of physical terminology in remote sensing community (Schaeppman-Strub

et al., 2006). This study would be the first step towards bringing additional clarity in the nighttime remote sensing community around remote sensing quantities that are traceable and fit to the scientific questions such as anisotropy of ALAN. As such, radiant intensity could be employed as a new standard product to systematically measure ALAN in daily, monthly and annual time scales. This assumes that the products have been carefully compensated for extraneous sources of light emissions. Such an effort, would lead to improved access to the already-rich information content embedded in multi-angular VIIRS DNB radiances.

### CRediT authorship contribution statement

**Xi Li:** Conceptualization, Methodology, Writing – original draft, Writing – review & editing, Funding acquisition, Software. **Xiaoyu Shang:** Software, Data curation. **Qingling Zhang:** Conceptualization, Methodology. **Deren Li:** Conceptualization. **Fengrui Chen:** Resources, Data curation. **Minghui Jia:** Software, Data curation. **Yan Wang:** Software.

### Declaration of Competing Interest

The authors declare that they have no known competing financial interests or personal relationships that could have appeared to influence the work reported in this paper.

### Acknowledgement

This research was supported by the National Key R&D Program of China (Grant no. 2019YFE0126800) and National Natural Science Foundation of China (Grant no. 41771386).

### References

- Bennie, J., Duffy, J., Davies, T., Correa-Cano, M., Gaston, K., 2015. Global trends in exposure to light pollution in natural terrestrial ecosystems. *Remote Sens.* 7 (3), 2715.
- Cao, X., Chen, J., Imura, H., Higashi, O., 2009. A SVM-based method to extract urban areas from DMSP-OLS and SPOT VGT data. *Remote Sens. Environ.* 113 (10), 2205–2209.
- Cao, C., Shao, X., Upadhyay, S., 2013. Detecting light outages after severe storm using the Suomi NPP/VIIRS day/night band radiances. *IEEE Geosci. Remote Sens. Lett.* 10 (6), 1582–1586.
- Chen, X., Nordhaus, W.D., 2011. Using luminosity data as a proxy for economic statistics. *Proc. Natl. Acad. Sci.* 108 (21), 8589–8594.
- Cinzano, P., Castro, F., 1998. The Artificial Sky Luminance and the Emission Angles of the Upward Light Flux arXiv preprint astro-ph/9811297.
- Coesfeld, J., Anderson, S.J., Baugh, K., Elvidge, C.D., Schernthanner, H., Kyba, C.C.M., 2018. Variation of individual location radiance in VIIRS DNB monthly composite images. *Remote Sens.* 10 (12).
- Croft, T.A., 1978. Nighttime images of the Earth from space. *Sci. Am.* 239, 86–98.
- Elvidge, C., Baugh, K., Hobson, V., Kihn, E., Kroehl, H., Davis, E., Cocero, D., 1997. Satellite inventory of human settlements using nocturnal radiation emissions: a contribution for the global toolchest. *Glob. Chang. Biol.* 3 (5), 387–395.
- Elvidge, C.D., Sutton, P.C., Ghosh, T., Tuttle, B.T., Baugh, K.E., Bhaduri, B., Bright, E., 2009. A global poverty map derived from satellite data. *Comput. Geosci.* 35 (8), 1652–1660.
- Elvidge, C.D., Baugh, K.E., Zhizhin, M., Hsu, F.-C., 2013. Why VIIRS data are superior to DMSP for mapping nighttime lights. In: Proceedings of the Asia-Pacific Advanced Network. Hawaii, USA, 12–13 January 2013.
- Elvidge, C.D., Hsu, F.-C., Zhizhin, M., Ghosh, T., Taneja, J., Bazilian, M., 2020. Indicators of electric power instability from satellite observed nighttime lights. *Remote Sens.* 12 (19), 3194.
- Filonchik, M., Yan, H., Zhang, Z., Yang, S., Li, W., Li, Y., 2019. Combined use of satellite and surface observations to study aerosol optical depth in different regions of China. *Sci. Rep.* 9 (1), 1–15.
- Garstang, R., 1986. Model for artificial night-sky illumination. *Publ. Astron. Soc. Pac.* 98 (601), 364–375.
- Henderson, V., Storeygard, A., Weil, D.N., 2011. A bright idea for measuring economic growth. *Am. Econ. Rev.* 101 (3), 194–199.
- Kocifaj, M., 2018. Towards a comprehensive city emission function (CCEF). *J. Quant. Spectrosc. Radiat. Transf.* 205, 253–266.
- Kocifaj, M., Lamphar, H.A.S., 2016. Angular emission function of a city and skyglow modeling: a critical perspective. *Publ. Astron. Soc. Pac.* 128 (970), 124001.
- Kocifaj, M., Solano Lamphar, H.A., Kundracik, F., 2015. Retrieval of Garstang's emission function from all-sky camera images. *Mon. Not. R. Astron. Soc.* 453 (1), 819–827.
- Kyba, C.C., Kuester, T., de Miguel, A.S., Baugh, K., Jechow, A., Höller, F., Bennie, J., Elvidge, C.D., Gaston, K.J., Guanter, L., 2017. Artificially lit surface of Earth at night increasing in radiance and extent. *Sci. Adv.* 3 (11), e1701528.
- Kyba, C.C., Aubé, M., Bará, S., Bertolo, A., Bouroussis, C.A., Cavazzani, S., Espey, B.R., Falchi, F., Gyuk, G., Jechow, A., et al., 2021a. The benefit of multiple angle observations for visible band remote sensing using night lights. In: *Earth and Space Science Open Archive ESSOA* (preprint).
- Kyba, C., Ruby, A., Kuechly, H., Kinney, B., Miller, N., Sanders, J., Barentine, J., Kleinodt, R., Espey, B., 2021b. Direct measurement of the contribution of street lighting to satellite observations of nighttime light emissions from urban areas. *Light. Res. Technol.* 53 (3), 189–211.
- Levin, N., 2017. The impact of seasonal changes on observed nighttime brightness from 2014 to 2015 monthly VIIRS DNB composites. *Remote Sens. Environ.* 193, 150–164.
- Levin, N., Kyba, C.C.M., Zhang, Q., Sánchez de Miguel, A., Román, M.O., Li, X., Portnov, B.A., Molthan, A.L., Jechow, A., Miller, S.D., Wang, Z., Shrestha, R.M., Elvidge, C.D., 2020. Remote sensing of night lights: a review and an outlook for the future. *Remote Sens. Environ.* 237, 111433.
- Li, X., Li, D., 2014. Can nighttime light images play a role in evaluating the Syrian Crisis? *Int. J. Remote Sens.* 35 (18), 6648–6661.
- Li, X., Xu, H., Chen, X., Li, C., 2013. Potential of NPP-VIIRS nighttime light imagery for modeling the regional economy of China. *Remote Sens.* 5 (6), 3057–3081.
- Li, X., Ma, R., Zhang, Q., Li, D., Liu, S., He, T., Zhao, L., 2019. Anisotropic characteristic of artificial light at night – Systematic investigation with VIIRS DNB multi-temporal observations. *Remote Sens. Environ.* 233, 111357.
- Li, X., Levin, N., Xie, J., Li, D., 2020. Monitoring hourly nighttime light by an unmanned aerial vehicle and its implications to satellite remote sensing. *Remote Sens. Environ.* 247, 111942.
- Liu, Z., He, C., Zhang, Q., Huang, Q., Yang, Y., 2012. Extracting the dynamics of urban expansion in China using DMSP-OLS nighttime light data from 1992 to 2008. *Landsc. Urban Plan.* 106 (1), 62–72.
- Lu, D., Tian, H., Zhou, G., Ge, H., 2008. Regional mapping of human settlements in southeastern China with multisensor remotely sensed data. *Remote Sens. Environ.* 112 (9), 3668–3679.
- Luginbuhl, C., Duriscoe, D., Morre, C., Richman, N., Lockwood, W., Davids, D., 2009. From the ground up II: sky glow and near-ground artificial light propagation in Flagstaff, Arizona. *Publ. Astron. Soc. Pac.* 121, 204–212.
- Mann, M.L., Melaas, E.K., Malik, A., 2016. Using VIIRS Day/Night band to measure electricity supply reliability: preliminary results from Maharashtra, India. *Remote Sens.* 8 (9).
- Miller, S.D., Straka, W., Mills, S.P., Elvidge, C.D., Lee, T.F., Solbrig, J., Walther, A., Heidinger, A.K., Weiss, S.C., 2013. Illuminating the capabilities of the suomi national polar-orbiting partnership (NPP) visible infrared imaging radiometer suite (VIIRS) day/night band. *Remote Sens.* 5 (12), 6717–6766.
- Román, M.O., Stokes, E.C., 2015. Holidays in lights: tracking cultural patterns in demand for energy services. *Earth's Future* 3, 182–205.
- Román, M.O., Wang, Z., Sun, Q., Kalb, V., Miller, S.D., Molthan, A., Schultz, L., Bell, J., Stokes, E.C., Pandey, B., Seto, K.C., Hall, D., Oda, T., Wolfe, R.E., Lin, G., Golpayegani, N., Devadiga, S., Davidson, C., Sarkar, S., Praderas, C., Schmaltz, J., Boller, R., Stevens, J., Ramos González, O.M., Padilla, E., Alonso, J., Detrés, Y., Armstrong, R., Miranda, I., Conte, Y., Marrero, N., MacManus, K., Esch, T., Masuoka, E.J., 2018. NASA's Black Marble nighttime lights product suite. *Remote Sens. Environ.* 210, 113–143.
- Román, M.O., Stokes, E.C., Shrestha, R., Wang, Z., Schultz, L., Carlo, E.A.S., Sun, Q., Bell, J., Molthan, A., Kalb, V., Ji, C., Seto, K.C., McClain, S.N., Enenkel, M., 2019. Satellite-based assessment of electricity restoration efforts in Puerto Rico after Hurricane Maria. *PLoS One* 14 (6), e0218883.
- Román, M.O., Wang, Z., Shrestha, R., Yao, T., Kalb, V., 2021. Black Marble User Guide Version 1.2.
- Rousseeuw, P.J., Leroy, A.M., 2005. Robust Regression and Outlier Detection. John Wiley & Sons.
- Sánchez de Miguel, A., Zamorano, J., Gómez Castaño, J., Pascual, S., 2013. Evolution of the energy consumed by street lighting in Spain estimated with DMSP-OLS data. *J. Quant. Spectrosc. Radiat. Transf.* 139, 109–117.
- Schaepman-Strub, G., Schaepman, M.E., Painter, T.H., Dangel, S., Martonchik, J.V., 2006. Reflectance quantities in optical remote sensing—Definitions and case studies. *Remote Sens. Environ.* 103 (1), 27–42.
- Sharma, R.C., Tateishi, R., Hara, K., Gharechelou, S., Iizuka, K., 2016. Global mapping of urban built-up areas of year 2014 by combining MODIS multispectral data with VIIRS nighttime light data. *Int. J. Digit. Earth* 9 (10), 1004–1020.
- Small, C., Elvidge, C.D., 2013. Night on Earth: mapping decadal changes of anthropogenic night light in Asia. *Int. J. Appl. Earth Obs. Geoinf.* 22, 40–52.
- Tong, K.P., Kyba, C.C.M., Heygster, G., Kuechly, H.U., Notholt, J., Kolth, Z., 2020. Angular distribution of upwelling artificial light in Europe as observed by Suomi-NPP satellite. *J. Quant. Spectrosc. Radiat. Transf.* 107009.
- Waluda, C.M., Griffiths, H.J., Rodhouse, P.G., 2008. Remotely sensed spatial dynamics of the *Illex argentinus* fishery, Southwest Atlantic. *Fish. Res.* 91 (2–3), 196–202.
- Wang, Z., Román, M.O., Kalb, V.L., Miller, S.D., Zhang, J., Shrestha, R.M., 2021. Quantifying uncertainties in nighttime light retrievals from Suomi-NPP and NOAA-20 VIIRS Day/Night Band data. *Remote Sens. Environ.* 263, 112557.
- Wolfe, R.E., Lin, G., Nishihama, M., Tewari, K.P., Tilton, J.C., Isaacman, A.R., 2013. Suomi NPP VIIRS prelaunch and on-orbit geometric calibration and characterization. *J. Geophys. Res.-Atmos.* 118 (20), 11,508–511,521.
- Xie, Y., Weng, Q., 2016. Updating urban extents with nighttime light imagery by using an object-based thresholding method. *Remote Sens. Environ.* 187, 1–13.

- Yu, B., Shi, K., Hu, Y., Huang, C., Chen, Z., Wu, J., 2015. Poverty evaluation using NPP-VIIRS nighttime light composite data at the county level in China. *Ieee J. Select. Top. Appl. Earth Observ. Remote Sens.* 8 (3), 1217–1229.
- Zhang, Q., Seto, K., 2011. Mapping urbanization dynamics at regional and global scales using multi-temporal DMSP/OLS nighttime light data. *Remote Sens. Environ.* 115 (9), 2320–2329.
- Zhao, X., Yu, B., Liu, Y., Yao, S., Lian, T., Chen, L., Yang, C., Chen, Z., Wu, J., 2018. NPP-VIIRS DNB daily data in natural disaster assessment: evidence from selected case studies. *Remote Sens.* 10 (10), 1526.
- Zhou, Y., Smith, S.J., Elvidge, C.D., Zhao, K., Thomson, A., Imhoff, M., 2014. A cluster-based method to map urban area from DMSP/OLS nightlights. *Remote Sens. Environ.* 147 (5), 173–185.